The Structure of the Free Neutron Via Spectator Tagging

A new Research Proposal to Jefferson Lab (PAC 23)

Gail Dodge, Alexei Klimenko, Sebastian Kuhn (co-spokesperson)*, Stepan Stepanyan, Lawrence Weinstein
Old Dominion University

Will Brooks, Volker Burkert, Rolf Ent, Howard Fenker, David Gaskell, Wally Melnitchouk (co-spokesperson), Mac Mestayer
Jefferson Lab

M. Eric Christy, Cynthia Keppel (co-spokesperson), Niatika Kittrell, Edwin Segbefia
Hampton University

Keith Griffioen
The College of William and Mary

Fabio Sauli
CERN

Ed Kinney
University of Colorado, Boulder

Claudio Ciofi degli Atti, Leonya Kaptari
Istituto Nazionale di Fisica Nucleare, Perugia, Italy

Boris Kopeliovich
Max-Planck Institut Heidelberg

Silvano Simula
Istituto Nazionale di Fisica Nucleare, Roma, Italy

Ioana Niculescu
James Madison University

Laird Kramer, Misak Sargsian
Florida International University

Marco Anghinolfi, Marco Battaglieri, Raffaella De Vita, Michail Osipenko, Gianni Ricco, Marco Ripani, Mauro Taiuti
Istituto Nazionale di Fisica Nucleare, Genova, Italy

Kim Egiyan
Yerevan Physics Institute, Armenia

Mark Strikman
Penn State University

Simonetta Liuti, Gabriel Niculescu
University of Virginia

John Arrington
Argonne National Lab

Maurik Holtrop
University of New Hampshire

Franz Klein
Catholic University

Luminita Todor
Carnegie Mellon University

Sabine Jeschonnek
Ohio State University

A CLAS collaboration proposal

* Contact: Sebastian Kuhn, Department of Physics, Old Dominion University, Norfolk VA 23529. Email: skuhn@odu.edu

Abstract

The structure of the proton has been studied in great detail through inelastic scattering for several decades. However, much less is known about the structure of the neutron, due to the unavailability of free neutron targets and the substantial theoretical uncertainties associated with extracting information from nucleons bound in nuclei. In order to overcome this problem, we propose a measurement of the inclusive electron scattering cross section on an almost free neutron using the CEBAF Large Acceptance Spectrometer (CLAS) and a novel technique to largely eliminate nuclear binding effects. We will use a low-momentum recoil detector to tag slow backward-moving spectator protons in coincidence with the scattered electron in the reaction $D(e, e'p_s)X$. This way we can ensure that the electron scattering reaction took place on an almost free neutron, and we can infer its initial four-momentum from the observed spectator proton. We propose to use this technique to extract the structure function F_2^n over a significant range in Q^2 (from about 1 to 5 GeV^2) and W (from the elastic peak to $W = 3$ GeV). We will use two beam energies (4 and 6 GeV) with in-bending CLAS torus field configurations. The kinematic coverage, which includes the elastic and resonance regions as well as part of the deep inelastic region (from $x = 0.2$ to 0.6), allows us to extract neutron elastic form factors, resonance excitation strengths, and the ratio F_2^n/F_2^p at high x. These data will also allow us to test quark-hadron duality for the neutron for the first time. This experiment requires the development and construction of a novel recoil detector with low momentum threshold ($\leq$ 70 MeV/c) for protons and high rate capability. We will use the solenoid under development for the approved DVCS experiment to sweep out Møller background. CLAS will be used in its standard configuration with luminosities up to $0.5 \cdot 10^{34}$ cm^{-2}s^{-1}, but with the large angle drift chambers turned off. We request a total of 40 days of new beamtime in Hall B (20 days at 6 GeV, 10 days at 4 GeV, 5 days of background test and calibration runs, and 5 days of engineering for the new recoil detector).

Contents

1 Introduction

This proposal pioneers a new experimental technique at Jefferson Lab (JLab) for low- momentum target recoil detection in coincidence with high-energy electron scattering. We propose to build a novel time-projection-chamber-like recoil detector, which in combination with sufficiently thin targets will allow us to detect protons down to momenta below 70 MeV/c, and other nuclear fragments to correspondingly low momenta. We are also considering an enhancement of this detector with a neutron array for low-momentum neutrons.

Although this apparatus will open up a vast field of new experimental studies, the present proposal (dubbed "BONUS" for "Barely Off-shell NUcleon Structure") is focused on just one goal: to study the structure of free neutrons with comparable detail and precision as has been achieved for the proton at JLab. We will use the recoil detector and a thin deuterium target to tag scattering events on a loosely bound, nearly on-shell neutron by detecting slow protons emitted in the backward direction relative to the momentum transfer vector. Many additional experiments are possible with other nuclear targets and other detected nuclear fragments, which explore topics from the high-momentum structure of light nuclei to coherent production of mesons. Corresponding plans are being developed for future proposals.

Structure functions of the nucleon reflect the defining features of QCD: asymptotic freedom at large momenta and small distance scales, as well as confinement and non-perturbative effects at the hadronic scale. From measurements of these structure functions in the scaling region, one can infer the momentum and spin carried by the quarks and by the gluons (via perturbative evolution) inside the nucleon. At the same time, through violations of scaling and power corrections to the leading-twist structure functions, one gains access to the non-perturbative quark-gluon dynamics in a bound hadronic system. Resonance excitation strengths can be compared to QCD-inspired models and eventually to lattice calculations of baryon structure. The link between the resonance structure and the quark structure at high energies can be explored by studying the applicability and limits of quark-hadron duality in inclusive structure functions.

One of the most interesting open questions in nucleon structure is what happens to the structure functions as Bjorken x approaches unity, and nearly all of the nucleon momentum is carried by a single quark. This limit is dominated by the relative contributions of the u and d valence quarks. Simple phenomenological models like the SU(6) symmetric quark model predict significantly different behavior than perturbative QCD or quark models with improved hyperfine interactions. A quantity which is particularly sensitive to different symmetry breaking mechanisms in this region is the ratio of the neutron and proton unpolarized structure functions F_2^n/F_2^p. Although F_2^p is well known, F_2^n can only be deduced using nuclear targets which for inclusive experiments requires models for the nuclear physics and a subtraction of the F_2^p background.

Another interesting question is whether Bloom-Gilman duality holds as well for the neutron as it does for the proton. The beautiful JLab data for F_2^p, F_1^p and F_L^p in the resonance region show remarkable agreement with extrapolations of the deep-inelastic results to lower Q^2 at comparable x, when one averages over the resonance peaks. No such precise comparison has yet been possible for the neutron. The main stumbling block has been the absence of precise neutron data in the resonance region, where Fermi motion and off-shell effects wash out most of the resonance structure in inclusive electron scattering from a deuteron target.

A better knowledge of neutron structure functions in the resonance region is also urgently needed to extract the full isospin structure of resonant and non-resonant contributions to the cross section, and to interpret polarized structure function measurements as well as nuclear structure function measurements in this kinematic domain.

Finally, measurements of elastic scattering cross sections on the neutron provide valuable information on form factors in an independent and complementary approach to the existing JLab experiments (E94-017 in Hall B and E93-026 and E93-038 in Hall C).

In this proposal to the JLab Program Advisory Committee, we focus on measurements of the inclusive neutron structure functions at moderate to high x, including the resonance and elastic region, with detection of a slow backward-going spectator proton. We concentrate on inclusive scattering of 4 and 6 GeV electrons; however, many semi-inclusive and exclusive channels (*e.g.*, pion production) can be studied at the same time with this technique.

Future extensions to lower or higher beam energy and other targets or other final states are expected. We note that the proposed recoil detector will also serve as a valuable asset for the future program of the upgraded CLAS detector with 11 GeV beams. We will be able to extend the program of structure function measurements proposed here to higher Q^2 and x, up to $x \approx 0.85$ in the deep inelastic (DIS) region.

The proposal is based on the letter of intent we submitted to PAC22, which encouraged us to develop a full proposal. In the following pages, we explain the theoretical motivation and experimental method in more detail. We then describe the planned target-detector system and results from preliminary simulations and from the related experiment 94-102. We conclude with a summary and our beam time request to the PAC.

2 Physics Motivation

Although most of the existing nucleon structure data—from elastic form factors to deep inelastic structure functions—come from decades of experiments on readily available proton targets, measurements on the neutron are essential for a complete understanding. A complete determination of the valence content of the nucleon can be achieved only when both its u and d quark distributions are known, which, in the absence of high-precision neutrino data, necessarily requires information on the structure of the neutron. The absence of free neutron targets has meant that, until now, the usual method for extracting neutron structure information has been to use deuterium targets, and apply nuclear corrections arising from the Fermi motion and binding of the nucleons in the deuteron. Although this is sufficient in some cases, for many neutron observables, especially ones sensitive to the high momentum components of the deuteron wave function, the nuclear model uncertainties can be rather large. As a result, our knowledge of the structure of the neutron, especially in the neutron resonance region, and in the deep inelastic region at large x, is inadequate. Given the extremely high quality of proton data that are being accumulated at JLab and other facilities, obtaining a similar level of accuracy for the structure of the free neutron is a high priority. The new technique presented in this proposal allows us to access the structure of the free neutron with unprecedented accuracy, and with a minimum of uncertainty associated with nuclear corrections. This opens up a completely new program of measurements on the neutron, in analogy with those which have been carried out in the past on the proton. In

this section we highlight several examples which would benefit dramatically from a more accurate determination of the structure of the free neutron.

2.1 Neutron resonance structure

Resonance transition form factors provide fundamental information on the structure of the nucleon. The excited nucleon spectrum, and the associated $N \to N^*$ transition matrix elements, have provided benchmarks by which the quark model of the nucleon was initially established, and its various more recent extensions tested [1]. Although an impressive amount of data has been accumulated on proton transitions through measurements of structure functions in the resonance region, almost nothing is known about the nature of the resonance excitations of the neutron.

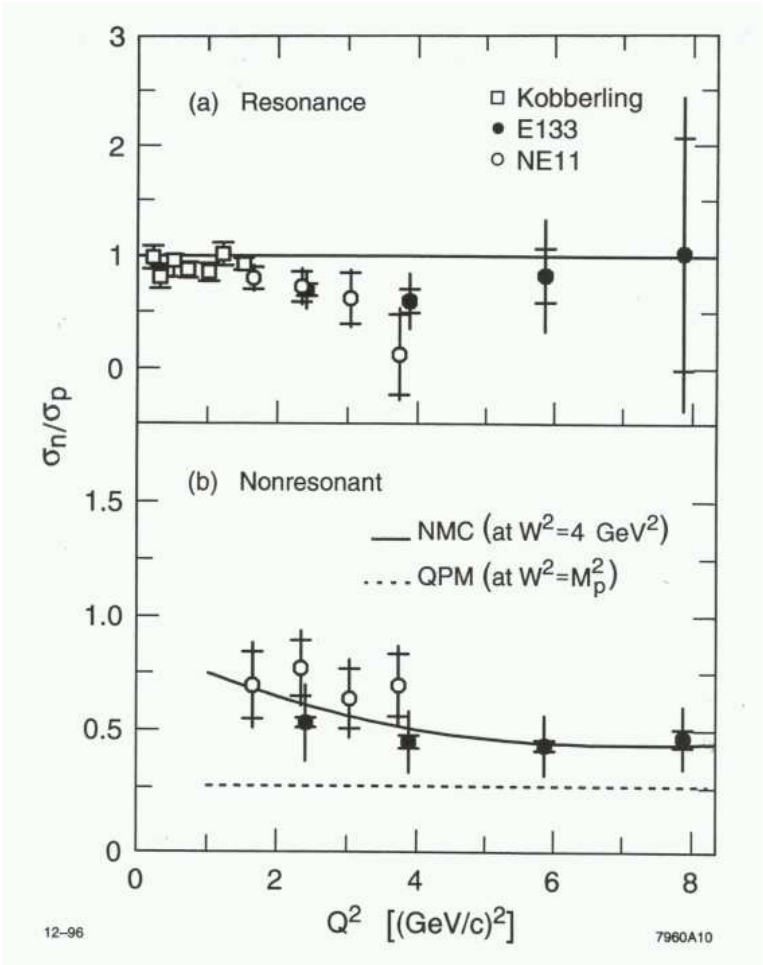

Figure 1: Extracted resonant and non-resonant contributions to the neutron to proton cross section ratio in the region of the Δ resonance [2]. The curves are from Refs. [3, 4].

In the limit of vanishing width, the contribution of an N^* resonance to the unpolarized F_1 and F_2 structure functions of the nucleon can be written as [5]

$$F_1 \;=\; M^2 \left(|G_+|^2 + |G_-|^2\right) \delta(W^2 - M_{N^*}^2) \qquad \text{and} \tag{1}$$

$$F_2 \;=\; (1+\nu^2/Q^2)^{-1} M\nu \left(|G_+|^2 + 2|G_0|^2 + |G_-|^2\right) \delta(W^2 - M_{N^*}^2) \;, \qquad (2)$$

in which the helicity amplitudes $G_m(m = \pm 1, 0)$ are defined in terms of $N \to N^*$ transition matrix elements:

$$G_m \;\propto\; \langle N^*, \lambda' = m - 1/2 | \epsilon_m^\mu \cdot j_\mu(0) | N, \lambda = 1/2 \rangle \;, \qquad (3)$$

with λ (λ') the helicity of the initial (final) state, ϵ_m^μ the photon polarization vector, and j_μ the electromagnetic current. The amplitudes $G_\pm$ are proportional to the helicity-conserving and helicity-flip amplitudes $A_{1/2}$ and $A_{3/2}$, respectively. The δ-function in Eqs. 1 and 2 for the sharp resonance can be replaced by a Breit-Wigner shape in practical fits to resonance data. For the $\Delta(1232)$ resonance, the extracted resonant and non-resonant contributions to the ratio of neutron to proton cross sections are depicted in Fig. 1 as a function of Q^2, from $Q^2 = 1$ to 8 GeV^2 [2]. No other high Q^2 neutron resonance electroproduction data exist. An average over all Q^2 yields $\sigma_n/\sigma_p = 0.72 \pm 0.07$ [2, 6] at the Δ resonance, whereas an average over low Q^2 data yields $\sigma_n/\sigma_p = 0.91 \pm 0.03$ [7].

The extracted neutron-Δ^0 transition form factor appears to be consistent with that of the proton-Δ^+ within the rather large uncertainties, and should therefore exhibit the same anomalous behavior seen in the proton data [8, 9, 10, 11]. Indeed, this would be expected for a pure Δ resonance contribution (and in fact for any isospin $I = 3/2$ excitation) in the limit of zero width, as in Eqs. 1 and 2, as isospin conservation constrains $I = 3/2$ amplitudes for the proton and neutron to be identical. In practice, however, a finite width together with tails from other resonances give rise to a non-resonant background, and even though it is smaller for the $\Delta(1232)$ than for higher mass resonances, it will differ for the proton and neutron, especially at higher Q^2. A difference between $p \to \Delta^+$ and $n \to \Delta^0$ transition form factors would therefore provide the first hints about the isospin structure of the non-resonant background. For $I = 1/2$ transitions, on the other hand, such as to the Roper resonance or the negative parity $S_{11}(1535)$, measurement of the electro-excitation off the neutron would allow the first determination of the isospin dependence of resonance production. The largest uncertainty in extracting the neutron data depicted in Fig. 1 is in fact the assumed value of σ_n/σ_p for the as yet unmeasured S_{11} resonance. A relativistic constituent quark model prediction for the S_{11} resonance is approximately constant for $Q^2 > 1.5$ GeV^2 at $\sigma_n/\sigma_p = 0.3$ [12].

Although precision electron-proton scattering experiments have been performed in a straightforward manner with hydrogen targets, it has been necessary to infer experimental information on the structure of the neutron from nuclear (typically deuteron) data. The procedure of unfolding neutron data from inclusive nuclear cross sections, via the subtraction of Fermi motion effects and contributions from various nuclear constituents, leads to ambiguities dependent on the models and reaction mechanisms employed. This is particularly true for measurements in the resonance region at high x and moderate Q^2.

To illustrate this, consider the inclusive resonance electroproduction cross section spectra shown in Fig. 2. These data were obtained at JLab at $Q^2 = 1.5$ GeV^2 for hydrogen and deuterium targets at matched kinematics. Although the three prominent resonance enhancements are obvious in the hydrogen data, only a hint of the first (the $\Delta(1232)$) is identifiable in the deuterium data. At $Q^2 > 2$ GeV^2, no discernible structure remains in the deuterium data at all. Neutron extraction from such data requires careful modeling of the resonant and

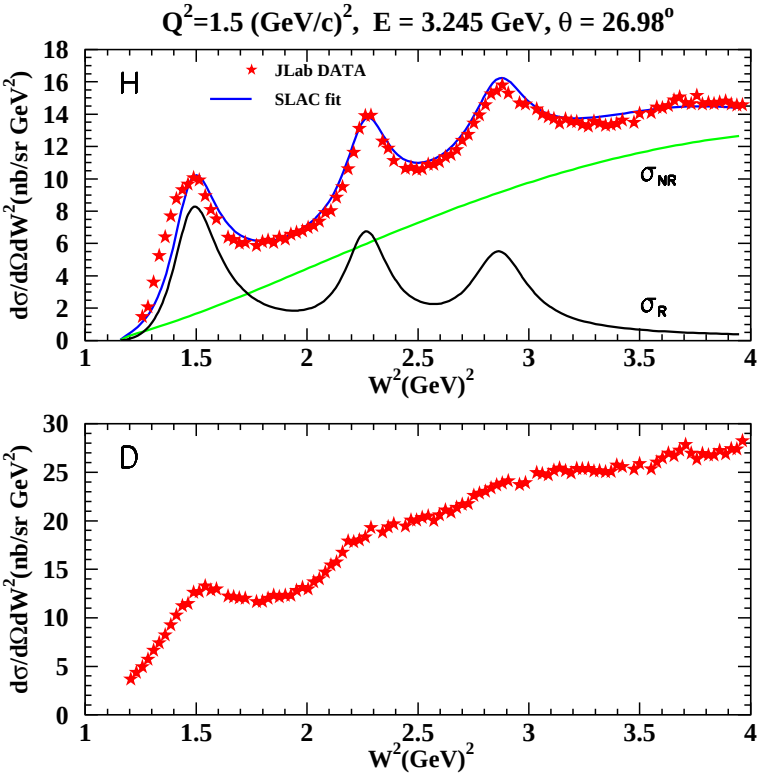

Figure 2: Inclusive resonance electroproduction cross sections from JLab at $Q^2 = 1.5$ GeV^2 [13]. Cross sections are shown as a function of invariant mass squared for hydrogen (top) and deuterium (bottom) targets at matched kinematics. The hydrogen spectrum is plotted with global resonant and non-resonant fits [3, 4].

non-resonant components for the neutron (as was done with the hydrogen data). Calculations must account for the nuclear effects of binding, Fermi motion, and nucleon off-shellness, and the model-dependence introduced by each of these steps leads to a substantial uncertainty in the neutron resonance structure functions. For instance, the deviation of σ_n/σ_p in Fig. 1 from unity in the Δ resonance region is most likely due to model uncertainties. For this reason, very little neutron resonance transition form factor data exist.

2.2 Quark-hadron duality for the neutron

The importance of the resonance region to the understanding of the quark structure of the nucleon is well known, and recent developments have emphasized this point even more emphatically. Measurements [13, 14, 15] at JLab of the unpolarized structure functions F_1 and F_2 on hydrogen, deuterium and nuclei in the resonance region have established to high accuracy the remarkable phenomenon of Bloom-Gilman duality down to $Q^2 \sim 0.5$ GeV^2. Also, HERMES has observed duality [16] in the proton spin asymmetry A_1. Namely, the structure functions in the resonance region at low W and Q^2 show a striking similarity, when averaged over resonances, to the scaling structure functions measured in the deep inelastic region at high W and Q^2. This phenomenon is even more remarkable given that the resonance-scaling duality appears to hold in each of the prominent resonance regions separately, indicating the presence of duality locally. Although a global version of duality, with integration over many resonances, can be qualitatively understood in the context of the twist expansion in QCD, at present the origin of local duality is unclear and the subject of considerable theoretical interest [17, 18].

The appearance of duality in QCD is usually taken to indicate that the size of higher twist contributions to structure functions, involving long-range correlations between quarks and gluons, is small [19]. As discussed by Close and Isgur [18], the higher twist effects are responsible for the difference between the scaling structure function expressed in terms of an incoherent sum of the squares of quark charges,

$$F_2(x) \;=\; x \sum_q e_q^2 \; q(x) \;, \tag{4}$$

and that given in terms of squares of form factors, Eqs. 1 and 2, involving a coherent sum over individual quark flavors,

$$|G_m|^2 \;=\; \left| \sum_q e_q \; G_m^{(q)} \right|^2 \;. \tag{5}$$

In the flavor-symmetric limit, the difference between these dual descriptions, which represents violations of Bloom-Gilman duality, is precisely due to the presence of higher twist effects. Diagrammatically these can be represented as off-diagonal quark transitions, in which the photon scatters from the nucleon with strength proportional to $\sum_{q \neq q'} e_q e_{q'}$. The experimental verification of Bloom-Gilman duality for the proton [20] implies that the single-quark scattering mechanism dominates the interaction above $Q^2 \sim 0.5$ GeV^2.

On the other hand, it has been observed that for the specific case of the proton, the sum over the off-diagonal contributions $\sum_{q \neq q'} e_q^{(p)} e_{q'}^{(p)} = 0$ simply because of the quark charge

assignments in the proton [18]. This leaves open the possibility that duality for the proton may not necessarily be an indication of suppression of higher twist effects, but merely the result of a fortuitous cancellation of coefficients. For the neutron, however, there is no such cancellation, since $\sum_{q \neq q'} e_q^{(n)} e_{q'}^{(n)} \neq 0$. Furthermore, within a simple harmonic oscillator quark model, Close and Isgur [18] find that the neutron structure functions should exhibit systematic deviations from local duality, and that duality should occur at higher W for the neutron than for the proton. Therefore, data on the neutron structure function in the resonance region are therefore vital.

Understanding duality could also prove to be crucial for mapping the transition from hadronic to quark-gluon degrees of freedom, and the measurements proposed here would allow one to identify the basic principles which underly this transition. Furthermore, if the systematics of Bloom-Gilman duality are understood quantitatively, duality could provide a powerful tool for accessing the scaling regime at large x. The proposed measurements would cover essentially the same Q^2 region as the original F_2^p experiment in Hall C [13] which so dramatically confirmed duality for the proton.

2.3 Deep inelastic scattering at large x

Above the resonance region, there are equally important reasons to want to understand the structure of the neutron. Although a large body of deep inelastic structure function data exists over a wide range of x and Q^2, the region $x > 0.6$ is not well explored. For $x \geq 0.4$ the contributions from the $\bar{q}q$ sea are negligible, and the structure functions are dominated by the valence quarks.

Knowledge of the valence quark distributions of the nucleon at large x is vital for several reasons. The simplest SU(6) symmetric quark model predicts that the ratio of d to u quark distributions in the proton is 1/2, however, the breaking of this symmetry in nature results in a much smaller ratio. Various mechanisms have been invoked to explain why the $d(x)$ distribution is softer than $u(x)$. If the interaction between quarks that are spectators to the deep inelastic collision is dominated by one-gluon exchange, for instance, the d quark distribution will be suppressed, and the d/u ratio will tend to zero in the limit $x \to 1$ [21]. This assumption has been built into most global analyses of parton distribution functions [22], and has never been tested independently. On the other hand, if the dominant reaction mechanism involves deep inelastic scattering from a quark with the same spin orientation as the nucleon, as predicted by perturbative QCD counting rules, then d/u tends to $\approx 1/5$ as $x \to 1$ [23]. Determining d/u experimentally would therefore lead to important insights into the mechanisms responsible for spin-flavor symmetry breaking. In addition, quark distributions at large x are a crucial input for estimating backgrounds in searches for new physics beyond the Standard Model at high energy colliders [24].

Because of the 4:1 weighting of the squared quark charges between the up and down quarks, data on the proton structure function, F_2^p, provide strong constraints on the u quark distribution at large x. In leading order,

$$F_2^p(x) \;=\; x \sum_q e_q^2 \, (q(x) + \bar{q}(x)) \;\approx\; x \left(\frac{4}{9} u(x) + \frac{1}{9} d(x) \right) \; . \tag{6}$$

The determination of the d quark distribution, on the other hand, requires in addition the

measurement of the neutron structure function, F_2^n. In particular, the d/u ratio can be determined (at leading order in α_s) from the ratio of neutron to proton structure functions,

$$\frac{F_2^n}{F_2^p} \approx \frac{1+4d/u}{4+d/u} , \tag{7}$$

provided $x \geq 0.4$ (at moderate to low Q^2) so that the sea quarks can be neglected. These kinematics are ideal for measurements at JLab.

In the past, data on F_2^n have been extracted primarily from inclusive scattering off deuterium. Unfortunately, theoretical uncertainties in the treatment of nuclear corrections have led to ambiguities in the extracted F_2^n at large x. In particular, inclusion of Fermi motion and nucleon off-shell corrections in the deuteron can lead to values for F_2^n/F_2^p which differ by 50% at $x = 0.75$, and by a factor $\sim$ 2–3 at $x = 0.85$ [25, 26, 27, 28]. This uncertainty is illustrated in Fig. 3, which shows F_2^n/F_2^p extracted from the *same* SLAC data on the proton and deuteron structure functions [25], with the nuclear corrections estimated on the basis of Fermi motion only (squares), taking nucleon off-shell effects into account [26, 28] (diamonds), and a model assuming suppression of point-like configurations (PLC) in the bound nucleon [28] (triangles). The latter is based on a simple relation between the EMC effect in the deuteron and heavy nuclei [28], and is valid only for $x \leq 0.75$ where the effects of Fermi motion are relatively small. The nuclear model dependence is as large or larger than the spread in the quark model predictions (arrows) as $x \to 1$. The tagged structure function method for measuring F_2^n proposed here virtually eliminates the uncertainties from nuclear models.

2.4 Neutron elastic scattering

The elastic form factors are basic observables that reflect the nucleon's composite nature. As with the transition form factors and deep inelastic structure functions, a considerable body of data now exists on the elastic electric and magnetic form factors of the proton, while the analogous form factors of the neutron are known much less accurately and over a more limited range of kinematics.

The magnetic form factor of the proton is reasonably well determined to $Q^2 = 30$ GeV^2. Accurate measurements of the neutron magnetic form factor, $G_M^n(Q^2)$, currently extend to $Q^2 \approx 5$ GeV^2, with plans to measure $G_M^n(Q^2)$ to $Q^2 \approx 14$ GeV^2 with an upgraded CLAS^{++} detector at the future 12 GeV CEBAF [29]. These experiments involve quasi-elastic scattering from the deuteron, with measurement of the ratio of scattered neutron to proton events to determine G_M^n/G_M^p. Unfortunately, quasi-elastic measurements at high Q^2 require more elaborate treatments of nuclear corrections, including the effects of relativity, final state interactions, and possible non-nucleonic degrees of freedom.

The nuclear corrections are even more problematic for extraction of the numerically smaller neutron electric form factor, G_E^n. An accurate determination of G_E^n at high Q^2 is vital for a number of reasons, not the least of which is the recent surprising result of a suppression of the proton electric form factor, G_E^p, relative to G_M^p at $Q^2 \sim$ 3–6 GeV^2 [30], and the need to verify whether similar behavior is exhibited by the neutron. Extraction of G_E^n from inclusive deuterium data has been plagued by overwhelming nuclear corrections

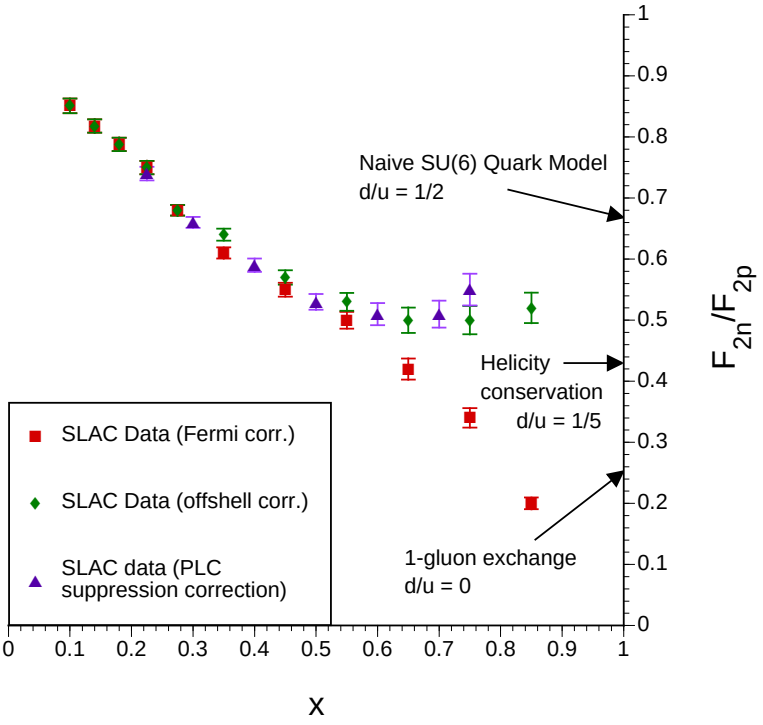

Figure 3: Neutron to proton structure function ratio, extracted from SLAC proton and deuteron data [25], assuming different prescriptions for the nuclear corrections, as described in the text. Several theoretical predictions for the $x \to 1$ limits are indicated by arrows.

associated with the deuteron wave function [31]. The corrections are more tractable in quasi-elastic scattering with neutron knockout from the deuteron or ^{3}He, but nevertheless they remain important, especially at high Q^2. The recent experiments at MAMI, Bates and JLab measuring double spin asymmetries in quasi-elastic scattering off deuterium and ^{3}He targets allow a nearly model-independent extraction of the *ratio* G_E^n/G_M^n, up to Q^2 of about 1.5 GeV^2. In future experiments, this method will be extended to even higher Q^2. However, to extract absolute values of either G_E^n or G_M^n, one needs to measure cross sections. The availability of a nearly free neutron target for cross section measurements will enable one to measure different combinations of G_E^n and G_M^n at high Q^2, essentially free from uncertainties from nuclear effects as well as neutron detection efficiencies.

3 Tagged structure functions

3.1 Spectator tagging

The measurement of tagged structure functions in semi-inclusive deep inelastic scattering (DIS) from the deuteron with a slow recoil proton detected in the backward hemisphere, $e + D \to e + p + X$, will allow the resolution of the ambiguities introduced by nuclear model dependence both in the deep inelastic and resonance (including elastic) regions [32, 33, 34]. Within the nuclear impulse approximation, in which the inelastic scattering takes place incoherently from individual nucleons, the differential semi-inclusive cross section can be written as a product of the deuteron spectral function, $\mathcal{S}$, and an effective (bound) neutron structure function, $F_2^{n(eff)}$ [34]:

$$\frac{d\sigma}{dx dW^2 d\alpha d^2p_T} \approx \frac{2\alpha_{em}^2(1-\nu/E)}{Q^4}\, \alpha\, \mathcal{S}(\alpha, p_T)\, F_2^{n(eff)}(W^2, p^2, Q^2)\ . \tag{8}$$

(For the full expression for the differential cross section in terms of the transverse and longitudinal structure functions see Ref. [34].) Here E is the initial electron energy, and ν the energy transfer; $W^2 = (p_d + q - p_s)^2$ is the invariant mass squared of the unobserved hadronic final state, with p_s the momentum of the spectator proton, p_d the momentum of the initial state deuteron, and $p = p_d - p_s$ the momentum of the struck neutron. The variable $\alpha = (E_s - p_s^z)/M$ is the light-cone momentum fraction carried by the spectator proton, p_T is its transverse momentum component (perpendicular to the direction of $\vec{q}$), $E_s = \sqrt{M^2 + \vec{p}_s^{\,2}}$ is its energy, and M is its mass. The use of the light-cone variable α emphasizes the kinematic dependence of the structure function at high Q^2, since $F_2^{n(eff)}(W^2, p^2, Q^2) \equiv F_2^{n(eff)}(x/(2-\alpha), p_T, Q^2)$. In addition, as discussed in Section 3.2.3 below, the dependence on α is only weakly affected by final state interactions. The degree to which the struck neutron is off-shell is given by

$$M^2 - p^2 \approx 2\vec{p}_s^{\,2} + 2M|\epsilon|\ , \tag{9}$$

where ϵ is the deuteron binding energy. In the limit $p^2 \to M^2$ (and $\alpha \to 1$), the effective neutron structure function $F_2^{n(eff)}(W^2, Q^2, p^2) \to F_2^n(W^2, Q^2, M^2) \equiv F_2^n(x, Q^2)$, the free neutron structure function. The p^2 dependence of $F_2^{n(eff)}$ depends somewhat on the theoretical assumptions made about the off-shell behavior of the photon-bound nucleon scattering

amplitude [35]. To avoid these uncertainties one therefore needs to minimize the degree to which the struck neutron is off-shell, by restricting oneself to small values of the spectator proton momentum, p_s. At the low momenta proposed in this experiment the uncertainty associated with the choice of deuteron wave function (or the spectral function, $\mathcal{S}$) is also expected to be quite small.

3.2 Backgrounds

The choice of backward kinematics for the spectator proton serves to minimize effects from final state interactions, as well as independent target fragmentation, while the restriction to small proton momenta mostly eliminates uncertainties associated with the deuteron wave function and on-shell extrapolation. In this section we consider each of these corrections to the impulse approximation in Eq. 8 explicitly. Corrections to the impulse approximation from the breaking of the factorization in Eq. 8 were analyzed in Ref. [36] for the inclusive deuteron structure function, and found to be quite small ($\leq 1\%$) for the kinematics considered here. The total estimated errors to F_2^n resulting from these corrections are given in Section 5.5.

3.2.1 Target fragmentation

The production of low momentum protons originating from the hadronic debris of the struck neutron is minimized by enforcing a large rapidity gap between the recoil proton and the rest of the hadronic debris [33, 37]. Although in the forward hemisphere (current fragmentation region) there are potentially large contributions from direct quark to proton fragmentation, especially at low x, in the backward hemisphere (target fragmentation) these are strongly suppressed. The direct fragmentation contribution is also expected to decrease with decreasing spectator proton momentum.

These features are evident from Fig. 4, where the ratio of the plane wave impulse approximation (PWIA), corrected for target fragmentation, to the pure PWIA contribution is shown as a function of the recoil angle, θ_{pq}, of the proton relative to the photon direction. Clearly, the effects of target fragmentation are relevant only in the forward hemisphere, and are totally negligible for $\theta_{pq} > 90^\circ$, even for large p_s.

3.2.2 Off-shell corrections

In order to minimize theoretical uncertainties associated with extrapolation of the semi-inclusive cross section to the nucleon pole, it is important that the tagged structure functions be measured for kinematics where the difference $p^2 - M^2$ is as small as possible. To assess the potential model dependence of the extracted neutron structure function on the extrapolation procedure we consider several models based on rather different dynamical assumptions.

In convolution models, off-shell corrections that appear at leading twist originate kinematically, as a consequence of the nucleon's transverse motion in the nucleus, and dynamically, from modifications of the bound nucleon structure. Kinematic off-shell effects can be calculated with very little model dependence, as discussed in Ref. [38], for instance. Dynamical off-shell effects, on the other hand, depend on descriptions of the intrinsic deformation of the bound nucleon structure, and are therefore more model-dependent.

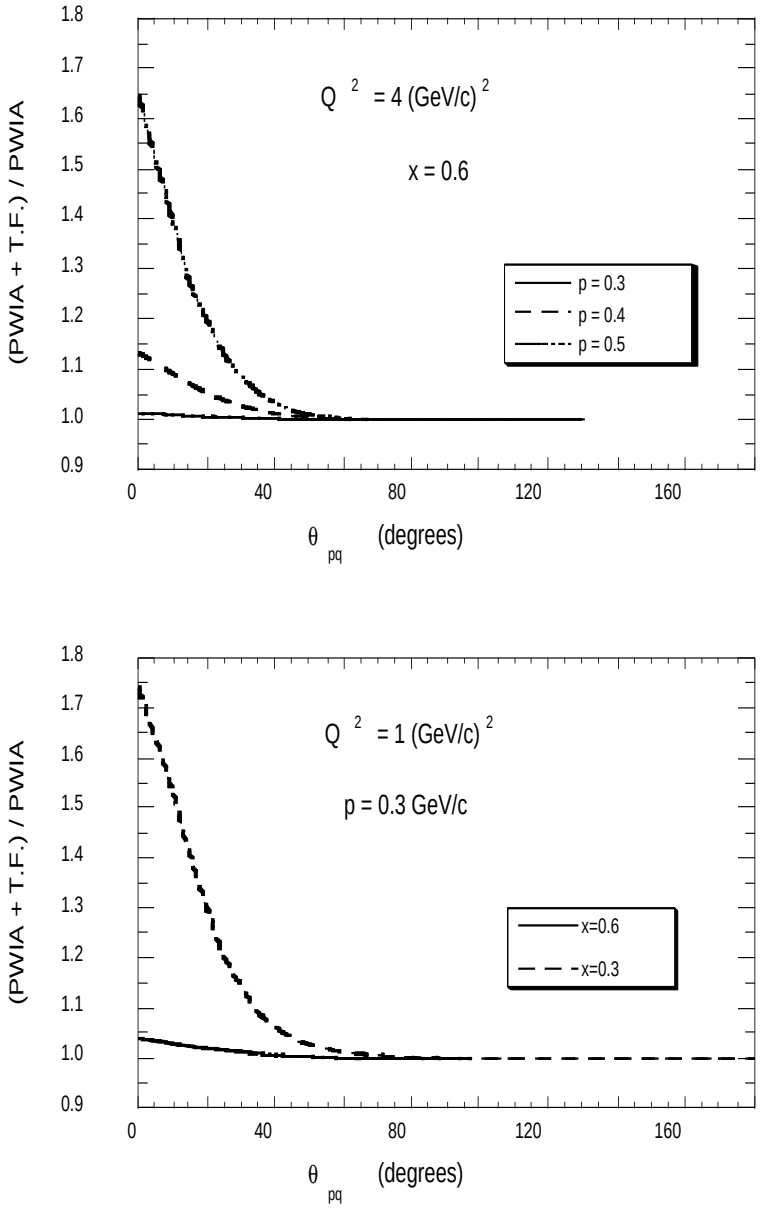

Figure 4: Effect of target fragmentation (TF) on the plane wave impulse approximation (PWIA) calculation of semi-inclusive DIS from the deuteron [33], as a function of the c.m. angle, θ_{pq}, between the spectator proton and the virtual photon.

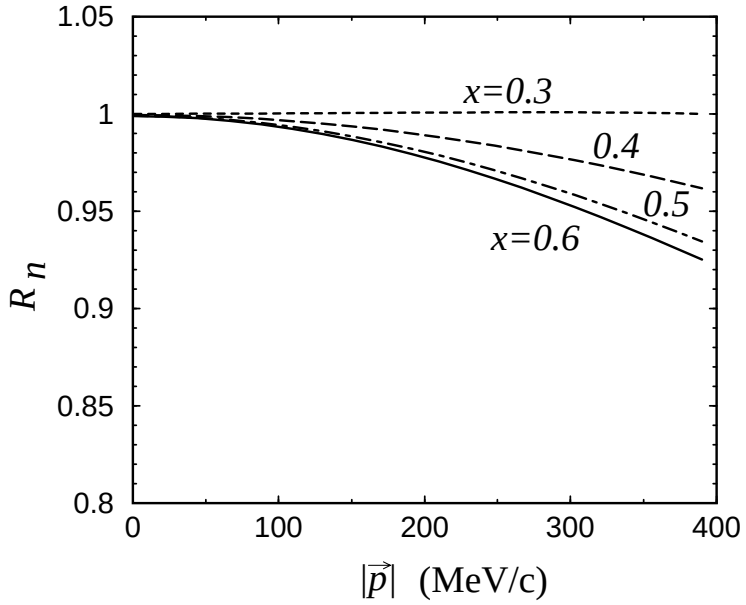

Figure 5: Ratio $R_n \equiv F_2^{n(eff)}(W^2, Q^2, p^2)/F_2^n(W^2, Q^2)$ of the bound to free neutron structure functions, as a function of the spectator proton momentum, in the model of Ref. [36].

In the covariant spectator model of Ref. [36], the DIS from a bound nucleon is described in terms of relativistic vertex functions that parameterize the nucleon-quark-diquark interaction (where "diquark" here refers to a system of a nucleon with one quark removed). The dependence of the vertex functions on the quark momentum and the diquark energy is constrained by fitting to the on-shell nucleon (proton) structure function data. The additional dependence of the vertex function on the virtuality of the off-shell neutron is fixed by comparing the calculated deuteron structure function with the inclusive F_2^d data. The resulting ratio $R_n \equiv F_2^{n(eff)}(W^2, Q^2, p^2)/F_2^n(W^2, Q^2)$ of the bound to free neutron structure functions is shown in Fig. 5 as a function of the momentum of the spectator proton, $|\vec{p}| = |\vec{p}_s|$, for several values of x. Here $Q^2 \sim 4$ GeV^2, although the Q^2 dependence is rather weak for $Q^2 > 1$ GeV^2. Not surprisingly, the effect at low $|\vec{p}_s|$ is very small, with the deviation from unity increasing at higher momenta. For $|\vec{p}_s| \approx 100$ MeV/c the effect is $\leq 1\%$ for $x = 0.6$, where the EMC effect is more pronounced, and essentially zero for $x = 0.3$.

A similar model in which the scattering from an off-shell nucleon is described in terms of a relativistic quark spectral function was introduced in Ref. [38]. In this approach the bound nucleon structure function is evaluated from the free nucleon structure function at a shifted value of the quark light-cone momentum fraction, which depends on the mass of the spectator diquark system, the bound nucleon momentum, and the binding energy [38]. The resulting ratio R_n of the bound to free neutron structure functions is shown in Fig. 6.

The deviation from unity is again small at low spectator proton momenta, amounting to $\leq 2\%$ for $|\vec{p}_s| \leq 100$ MeV/c, increasing to around 5% for $|\vec{p}_s| = 200$ MeV/c. In contrast to Fig. 5, however, the effect in this model is only weakly dependent on x. Similar behavior to that in Figs. 5 and 6 is also observed in the model of Ref. [39], where the assumption of weak binding in the deuteron allows one to calculate the off-shell dependence up to order p^2/M^2. An important constraint on the size of the nucleon's deformation in this approach

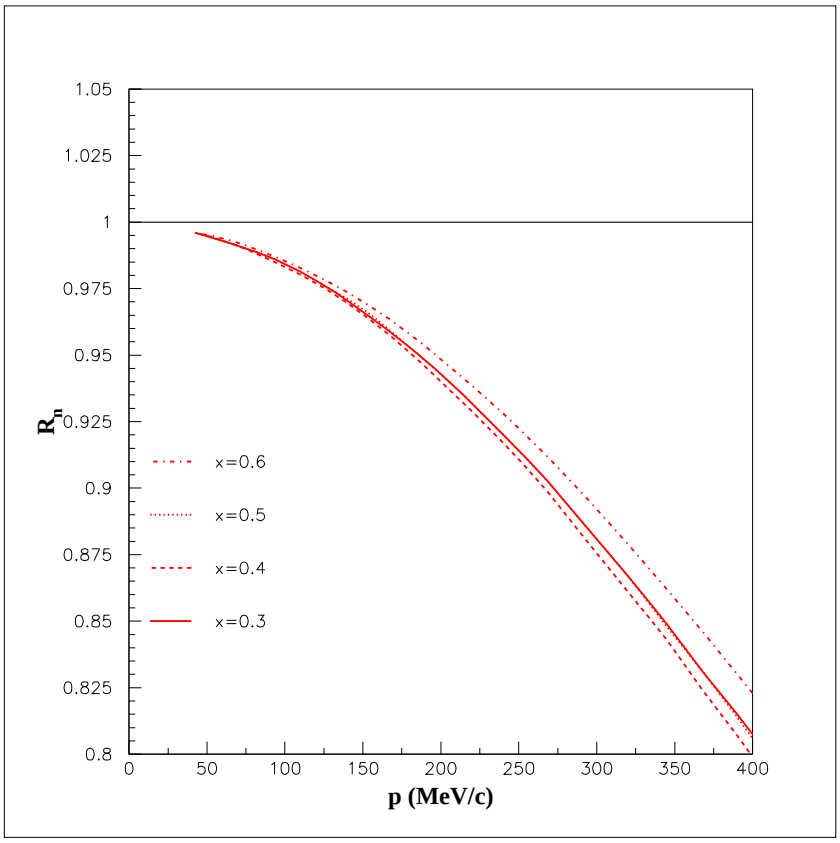

Figure 6: Ratio R_n of the bound to free neutron structure functions, as a function of the spectator proton momentum, in the model of Ref. [38].

is provided by the conservation of the number of valence quarks in the bound nucleon,

$$\frac{d}{dp^2}\int_0^1 dx\, q_{val}^{(eff)}(x, Q^2, p^2) = 0 \ , \tag{10}$$

where $q_{val}^{(eff)}$ is the valence quark distribution in the effective nucleon structure function, $F_2^{N(eff)}$. By imposing this constraint, one obtains an overall reduction of the kinematic off-shell effects whose strength can be located either at intermediate values of x, $x \geq 0.4$, as in the models of Refs. [36, 39], or at low values of x, $x \leq 0.15$, as suggested in Ref. [40].

Neglecting the contributions of $N\bar{N}$ pairs to the deuteron wave function, another estimate of the role of nucleon off-shellness can be made simply on the basis of kinematics. In the instant form approach discussed in Ref. [41], the nuclear structure function is related to the free nucleon structure function, evaluated at a shifted energy transfer, $\nu \to \bar{\nu}$, which depends on the degree to which the nucleon is bound (and hence, in the instant form language, off its energy shell). A shifted value of ν corresponds to a shifted value of x and Q^2 at which the nucleon structure function is evaluated. The ratio of the structure functions calculated in the plane wave impulse approximation with the modified variables (PWIA($\bar{q}$)) to that in which there is no modification is displayed in Fig. 7 as a function of θ_{pq} for $Q^2 = 1$ GeV^2. Once again, one sees that for low spectator proton momenta, $|\vec{p}_s| \approx 100$ MeV/c, the

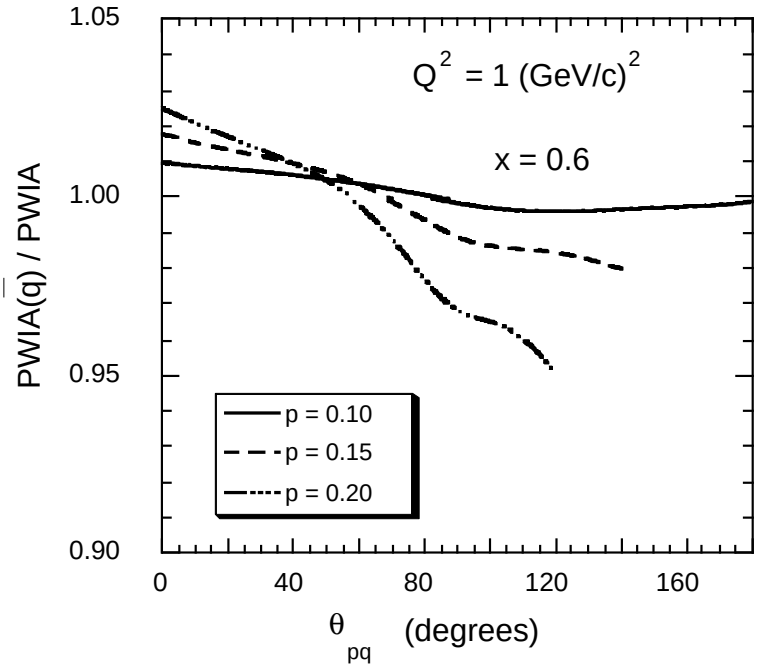

Figure 7: Ratio of bound to free nucleon structure functions, calculated using the model of Ref. [41]. The spectator proton momentum p is in units of GeV/c.

off-shell modification is less than 1% for all accessible angles. Only when one goes above $|\vec{p}_s| \approx 200$ MeV/c are there any effects at the $\leq 5\%$ level.

While the off-shell modification of the bound nucleon structure function in the above models is weak, the color screening model for the suppression of point-like configurations in bound nucleons [28] predicts somewhat larger deviations from unity of the ratio R_n than that in Figs. 5, 6 and 7. In this model one attributes most or all of the EMC effect to a medium modification of the internal structure of the bound nucleon, and little of the effect to mechanisms such as nuclear binding. On the other hand, since the deviation of the bound to free structure function ratio from the free limit is proportional to $2\vec{p}_s^{\,2} + 2M|\epsilon|$ (Eq. 9), sampling the data as a function of $\vec{p}_s^{\,2}$ should provide some guidance for a smooth extrapolation to the pole. In practice, considering a momentum interval of 70–200 MeV/c will allow the dependence on $\vec{p_s}^{\,2}$ to be constrained. Existing 6 GeV data from the JLab experiment E94-102 (E6) will in addition constrain the behavior of the bound structure function at larger $|\vec{p_s}^{\,2}|$ (for spectator momenta between ≈ 250 and 700 MeV/c).

Overall, we expect that the extrapolation from the minimum $|\vec{p}_s| \approx 70$ MeV/c, where the bound neutron is only around $M - \sqrt{|\vec{p_s}^{\,2}|} \approx 7$ MeV away from its mass-shell, should be relatively free of ambiguities. This is also supported by recent ^{4}He$(\vec{e}, e'\vec{p})$ polarization transfer experiments at Mainz and JLab [42] which indicate that the magnitude of the off-shell deformation may be rather small. These experiments measured the ratio of transverse to longitudinal polarization of the ejected protons, which is related to the medium modification of the electric to magnetic elastic form factor ratio. Using model independent relations derived from quark-hadron duality, one can relate the medium modifications in the form factors to a modification at large x of the deep inelastic structure function of the bound

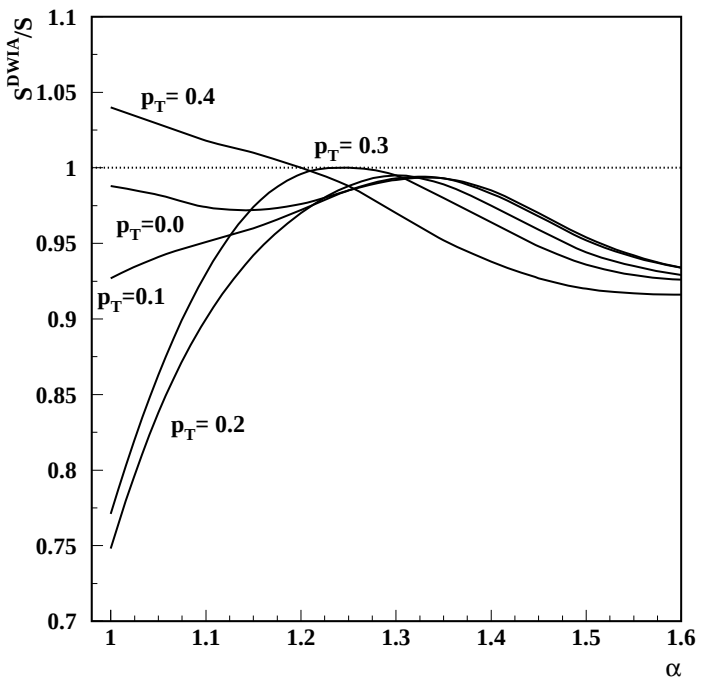

Figure 8: Spectral function calculated with and without FSI effects within the DWIA [34]. The curves correspond to different values of the spectator proton transverse momentum p_T (in GeV/c).

nucleon [43], which suggests an effect of $< 3\%$ for $x \leq 0.8$. The typical momentum of the knocked out protons in the experiments was ~ 50 MeV/c, although the results of the analysis were found not to depend strongly on the proton momentum [43]. These considerations lead us to expect that the extrapolation of the bound neutron structure function to the nucleon pole should introduce minimal uncertainty into the extracted structure function of the free neutron.

3.2.3 Final state interactions

Another possible source of uncertainty arises from final state interaction (FSI) effects, or rescattering of the spectator proton by the deep inelastic remnants, X, of the scattered neutron. The choice of backward angles is designed to minimize these effects. The magnitude of FSI effects has been estimated in several models, within the framework of the distorted wave impulse approximation (DWIA) [44], and in a string-like model which emphasizes the propagation and hadronization of the partonic debris emanating from the photon-bound nucleon vertex [45]. The strong suppression of FSIs at backward spectator proton angles is evident in both of these calculations.

A direct calculation of the FSI contribution to the cross section requires knowledge of the full dynamics of the spectator proton-X system. In the model of Ref. [44] the effects of FSIs are estimated by comparing with the calculation of FSI effects in the high-energy $^2\mathrm{H}(e, e'p)n$

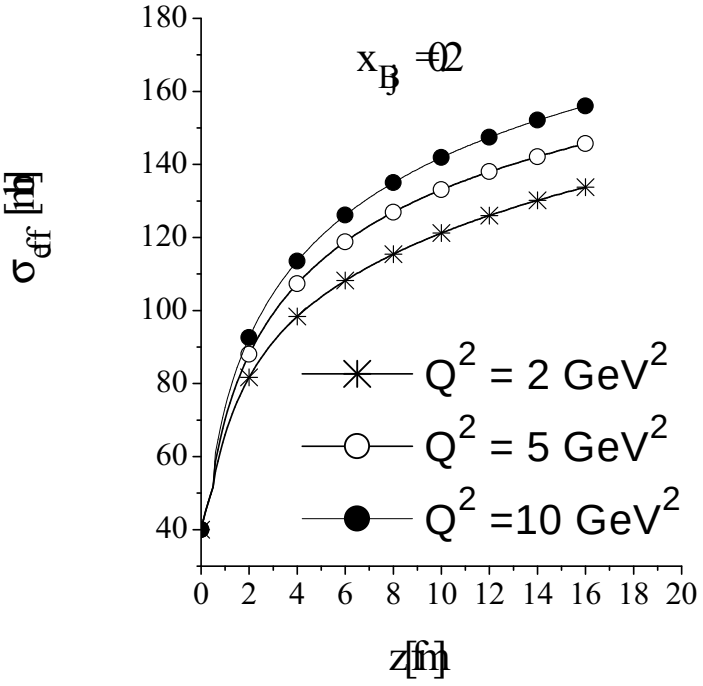

Figure 9: The debris-nucleon effective cross section, σ_{eff}, from Eq. 12 [48], as a function of the longitudinal distance z.

break-up reaction. The effective pX interaction cross section, σ_{eff}, is approximated [46] by that extracted from soft neutron production in the high-energy DIS of muons from heavy nuclei [47], $\sigma_{eff} \approx 20$ mb. The effect of the FSI is then to modify the spectral function $\mathcal{S} \to \mathcal{S}^{DWIA}$ [44], where

$$\mathcal{S}^{DWIA}(\alpha, p_T \approx 0) \sim \mathcal{S}(\alpha, p_T \approx 0) \left[1 - \frac{\sigma_{eff}(Q^2, x)}{8\pi \langle r_{pn}^2 \rangle} \frac{|\psi_d(\alpha, \langle p_T \rangle) \psi_d(\alpha, 0)|}{S(\alpha, p_T \approx 0)/\sqrt{E_s \; E_s(\langle p_T^2 \rangle)}} \right] , \quad (11)$$

with $\langle r_{pn}^2 \rangle$ the average separation of the nucleons within the deuteron, E_s the spectator energy, and $E_s(\langle p_T^2 \rangle) = \sqrt{M^2 + {p_s^z}^2 + \langle p_T^2 \rangle}$ the energy evaluated at the average transverse momentum ($\langle p_T^2 \rangle^{1/2} \sim$ 200–300 MeV/c) transferred for the hadronic soft interactions with effective cross section σ_{eff}. The steep momentum dependence of the deuteron wave function, $|\psi_d(\alpha, \langle p_T \rangle)| \ll |\psi_d(\alpha, p_T \approx 0)|$, ensures that FSI effects are suppressed in the extreme backward kinematics.

The effects of FSIs in this model are illustrated in Fig. 8, which shows the ratio of the light-cone spectral function including FSI effects within the DWIA to that without. At extreme backward kinematics ($p_T \approx 0$) one sees that FSI effects contribute less than $\sim 5\%$ to the overall uncertainty of the $d(e, e'n)X$ cross section for $\alpha \leq 1.5$. For $p_T = 0.1$ GeV/c the FSI effects are minimized at $\alpha = 1.3$, and remain at the $\leq 5\%$ level for values of α ($\alpha = 1.08$) typical in this experiment.

A more microscopic treatment of the effective rescattering cross section was also developed recently in Ref. [48]. Here the FSI due to the propagation of the struck nucleon debris

and its hadronization in the nuclear environment was applied to the $A(e,e'(A-1))X$ reaction, in which the residual $(A-1)$ nucleus is detected in coincidence with the scattered lepton. For a deuteron target, this process precisely coincides with that considered here, namely $^2\mathrm{H}(e,e'N)X$. The effective cross section, σ_{eff}, describing the interaction of the debris with a nucleon of the $(A-1)$ spectator system in this approach is both time- and Q^2-dependent.

In a color flux tube picture, once a quark is knocked out from a bound nucleon in the deuteron, a color field stretches between the quark and the remnants of the nucleon, which is then squeezed by the QCD vacuum into a color tube [49]. If the length of the tube is much greater than its transverse size, then it can resemble a colored string. In the adiabatic approximation, the interaction cross section of the string is expected to be of the order of typical hadronic total cross sections, $\sigma_{eff} \sim 20-40$ mb. On the other hand, as the string stretches, it may eventually break into two pieces, with the subsequent creation of $\bar{q}q$ pairs from the vacuum. As the string evolves and the process of string breaking continues, the number of produced hadrons increases with time, leading to an increased overall probability of interaction [48]. The effective interaction cross section σ_{eff} is therefore not constant, but grows logarithmically as a function of time, t.

Going beyond the adiabatic approximation, the deformation of the color string can also result in the radiation of gluons, which can subsequently decay to $\bar{q}q$ dipoles [50]. Assuming in turn that these dipoles give rise to mesons, this process produces an additional contribution to σ_{eff}, which also rises logarithmically with t. Including the effects of both color string breaking and gluon bremsstrahlung, the general expression for σ_{eff} has the form:

$$\sigma_{eff}(t) = \sigma_{tot}^{NN} + \sigma_{tot}^{\pi N}\Big[n_M(t) + n_G(t)\Big] \ , \tag{12}$$

in which σ_{tot}^{NN} and $\sigma_{tot}^{\pi N}$ are the total nucleon-nucleon and meson-nucleon scattering cross sections, and $n_M(t)$ and $n_G(t)$ are the effective numbers of created mesons and radiated gluons, respectively. The dependence of σ_{eff} on t (or equivalently on z, the longitudinal distance) and Q^2 is illustrated in Fig. 9 for $x = 0.2$. The rise of the interaction cross section with time (propagation length) is clearly evident. At larger x ($x \approx 0.5$) the effective cross section is reduced by $\approx 5\%$ in comparison.

Once the effective cross section of the interaction of the quark debris with the nucleons is defined, the standard eikonal approximation can be used to evaluate the cross section by replacing the struck nucleon momentum distribution with the distorted momentum distribution [51],

$$S^{PWIA}(\vec{p}_s) \to S^{FSI}(\vec{p}_s) = \frac{1}{3}\frac{1}{(2\pi)3}\sum_{\mathcal{M}_d}\left|\int d\vec{r}\ \Psi_{1,\mathcal{M}_d}(\vec{r})S(\vec{r})\chi_f^\dagger\ \exp(-i\vec{p}_s\cdot\vec{r})\right|^2 \ , \tag{13}$$

where the relative coordinate $\vec{r} = \vec{b} + z\vec{q}/|\vec{q}|$ is defined in terms of the longitudinal, z, and perpendicular, $\vec{b}$, components, with the z axis along $\vec{q}$. Here χ_f is the spin wave function of the final state, and $S(\vec{r})$ is the S-matrix describing the final state interaction between the debris and spectator nucleon,

$$S(\vec{r}) = 1 - \theta(z)\,\frac{\sigma_{eff}(z)(1-i\beta)}{4\pi b_0 2}\ \exp(-b^2/2b_0^2) \ , \tag{14}$$

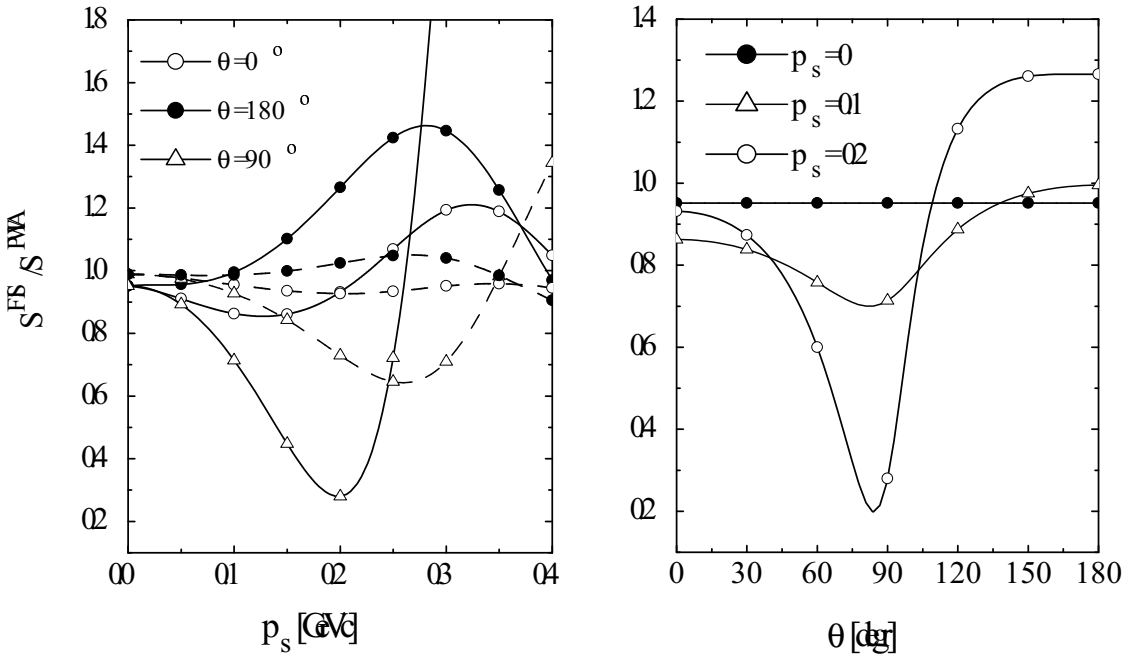

Figure 10: The momentum and angular dependence of the ratio S^{FSI}/S^{PWIA}, at $Q^2 = 5$ GeV^2 and $x = 0.2$ (after Ref. [52]). Left panel: dependence on spectator momentum, for the t and Q^2 dependent σ_{eff} (solid), and a constant $\sigma_{eff} = 20$ mb (dashed). Right panel: dependence on the angle between the spectator proton and the virtual photon direction.

where β is the ratio of the real to imaginary parts of the scattering amplitude, and the step function $\theta(z)$ arises from the high energy approximation of the Glauber theory. The above equations can also be used to calculate quasi-elastic scattering by replacing the debris-nucleon cross section with the nucleon-nucleon cross section.

The effects of FSIs in this model are illustrated in Fig. 10, where the ratio of spectral functions with and without FSI corrections is shown as a function of $|\vec{p}_s|$ and θ. The results using the t and Q^2 dependent effective cross section in Fig. 9, and those with a constant cross section $\sigma_{eff} = 20$ mb, are indicated in the left panel by the solid and dashed curves, respectively. For low spectator momenta, $|\vec{p}_s| \leq 100$ MeV/c, the effects at backward angles ($\theta \geq 130°$) are quite small, $\leq 5\%$, for both models. At larger momenta, $|\vec{p}_s| \approx 200$ MeV/c, FSIs introduce some 20–30% enhancement of the spectral function. The effects of FSIs become dominant at perpendicular angles, $\theta \sim 90°$, where for $|\vec{p}_s| = 200$ MeV/c they reduce the ratio of spectral functions by some 75%. In particular, the results are quite sensitive to the value of σ_{eff} at these angles, increasing the effect of FSIs by a factor 2–4 over the range $|\vec{p}_s| = 100$–200 MeV/c for the t-dependent cross section [48] compared with the smaller, constant $\sigma_{eff} = 20$ mb value. Of course, the study of FSIs and hadronization effects is interesting in its own right, and can be pursued by focusing on the kinematic region around $\theta \sim 90°$. On the other hand, the results of both the model calculations in Figs. 8 and 10 give us confidence that *even with* a relatively large uncertainty in σ_{eff}, the effects of FSIs at backward angles are less than 5% for $|\vec{p}_s| \leq 100$ MeV/c, and therefore constitute a small

correction to the impulse approximation in Eq. 8.

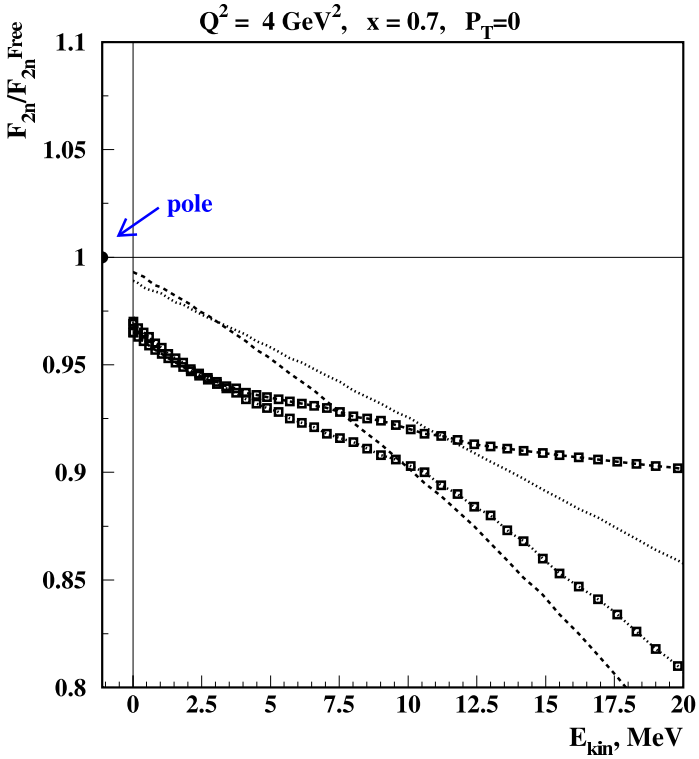

Figure 11: Effect of FSIs on the E_{kin} dependence of the extrapolated neutron structure function, normalized to the on-shell structure function, at extreme backward angles. The dashed and dotted lines represent the color screening [28] and color delocalization [53] models, respectively; the curves with the squares contain FSI effects.

The combined effects of FSIs and nucleon off-shell deformation on the extracted free neutron structure function are illustrated in Fig. 11, where we plot the effective F_2^n at $x = 0.7$ and $Q^2 = 4$ GeV^2 normalized to the free value as a function of the kinetic energy of the spectator proton, $E_{kin} = \vec{p}_s^{\,2}/2M$. The dashed and dotted lines represent the color screening [28] and color delocalization [53] models, respectively, and curves with the superimposed squares contain FSI effects calculated in the model of Ref. [44]. Since the off-shell effects in these models are generally larger than in the models of Figs. 5, 6 and 7, the size of the effect shown here is likely to be an upper estimate. For the proposed kinematics of this experiment, the range of spectator proton momenta would correspond to E_{kin} between 2.5 and 5 MeV. With several data points in this range, the measured tagged neutron structure function can then be extrapolated into the region of negative values of E_{kin}, in analogy with the Chew-Low procedure for extracting the pion cross section from $p(e, e'\pi)X$ data [54].

Since from Eq. 9 $M^2 - p^2 \approx 4M(|\epsilon|/2 + E_{kin})$, the pole of the off-shell neutron propagator (indicated in Fig. 11) in the PWIA amplitude is located at $E_{kin}^{pole} = -|\epsilon|/2$. The virtue of such an extrapolation is that, unlike the PWIA amplitude, the scattering amplitude containing final state interactions will not have a singularity at E_{kin}^{pole}. Thus, isolating the singularities through the extrapolation of effective structure functions into the negative spectator kinetic energy range will suppress the FSI effects in the extraction of the free F_2^n, independent of the model for the FSIs. Work on refining this procedure is currently under way [55]. Fig. 11 demonstrates that such an extrapolation can be done with the introduction of less than $\sim 2\%$ systematic error.

4 Experimental Setup and Recoil Detector

4.1 Proton Recoil Detector and Target

Figure 12 depicts the proposed proton recoil target–detector package situated in the Hall B CLAS spectrometer. The package consists of a thin deuterium target surrounded by a radial time projection chamber (RTPC) for the detection of low-momentum, backward-angle, recoil protons. The entire package is relatively small. The barrel is 20 cm long and about 13 cm in diameter. It will be situated at the standard Hall B target position, and inside the solenoid designed for the DVCS experiment (E01-113). Details of this new recoil detection system are discussed in detail below.

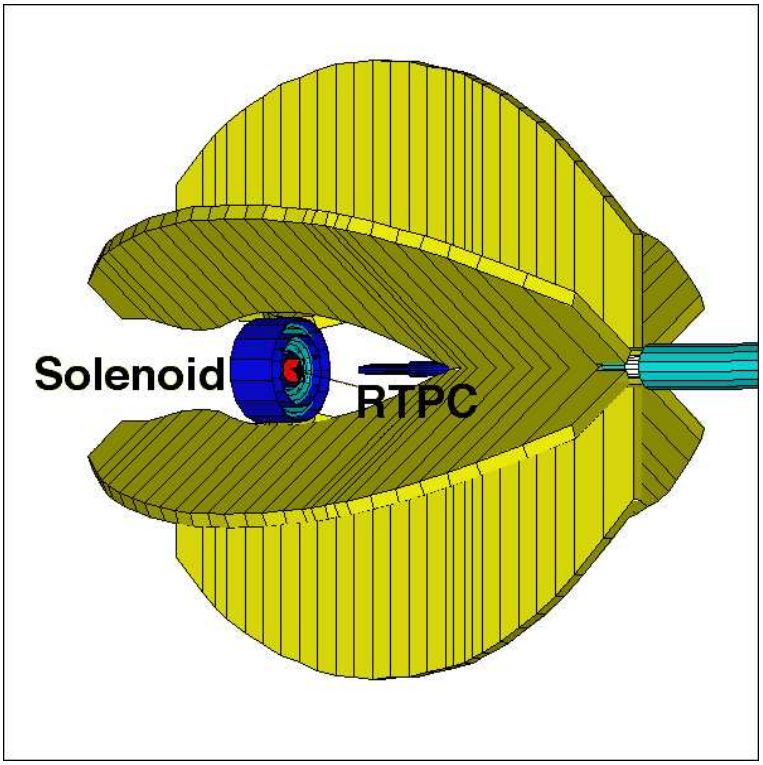

Figure 12: Thin deuterium target and radial TPC for proton detection shown inside CLAS using the planned DVCS solenoid.

4.2 Deuterium Target

Deuterium gas at 7.5 atm will be contained in a 4 mm diameter tube inside the recoil detector. The target tube will be 10 cm long, placed at the downstream end of the detector. This allows the detection of predominantly backward angle protons in the range 90-160 degrees. We plan to make the tube of readily-available 50 micron thick Kapton. Such a tube has been tested to 23 atm, the maximum possible in the available testing apparatus. Therefore, it may retain its structural integrity at even higher pressures. Work has also been done to develop thin (few micron) nickel foil target tubes, and these may provide a viable alternative to Kapton.

4.3 Møller Solenoid

Both the target and the spectator proton detector will be located inside the 30 cm long solenoid under development for the approved DVCS experiment E01-113 in CLAS. The longitudinal magnetic field from this solenoid will suppress Møller electron background in both the recoil detector and in the forward Region I drift chambers. It will also help us to separate tracks from low-momentum pions and other light particles from the spectator protons of interest, since the former will be bent sideways appreciably, leading to tracks that can be clearly identified with the proposed tracking detector.

Because the luminosity of the proposed experiment is much lower than that of E01-113, and because particles at small forward angles need not be detected, we can use a much lower magnetic field than the 5 T envisioned for E01-113. We assume a longitudinal field of 2 Tesla which would curl up all Møller electrons below 20 MeV/c before reaching our detection volume. However, our detector will work at much higher fields, and we can determine the optimum setting with beam on target.

4.4 Radial TPC Spectator Proton Tracking Detector

Low momentum spectator protons lose energy rapidly as they pass through matter, and therefore they leave short tracks or no tracks in solid detector components. In gas detectors however, ionization trails of significant length are readily achieved as the particles pass entirely through, or gradually slow down and stop, in the detection medium. Multiple measurements along a track provide a wealth of information about the particle that created it. Therefore, a promising spectator detector would be a gas chamber with appropriate geometry and minimal material. It would provide position and timing information sufficient to identify backwards-going particles and connect them to an outgoing electron detected in CLAS. Associated information about the particle's rate of energy loss (dE/dx) can provide compelling discrimination between protons and lighter charged particles.

A gas chamber configuration that provides all of these needs is a radial time projection chamber (RTPC). A diagram of the proposed detector is shown in Fig. 13. In outline, it consists of a pair of concentric cylinders with the annular space between the cylinders containing a sensitive gas. The cylinder's axis would be placed along the beamline. Charged particles produced at large (especially backwards) angles pass through the gas and leave a trail of electron-ion pairs. An electric field between the cylinders forces the electrons to

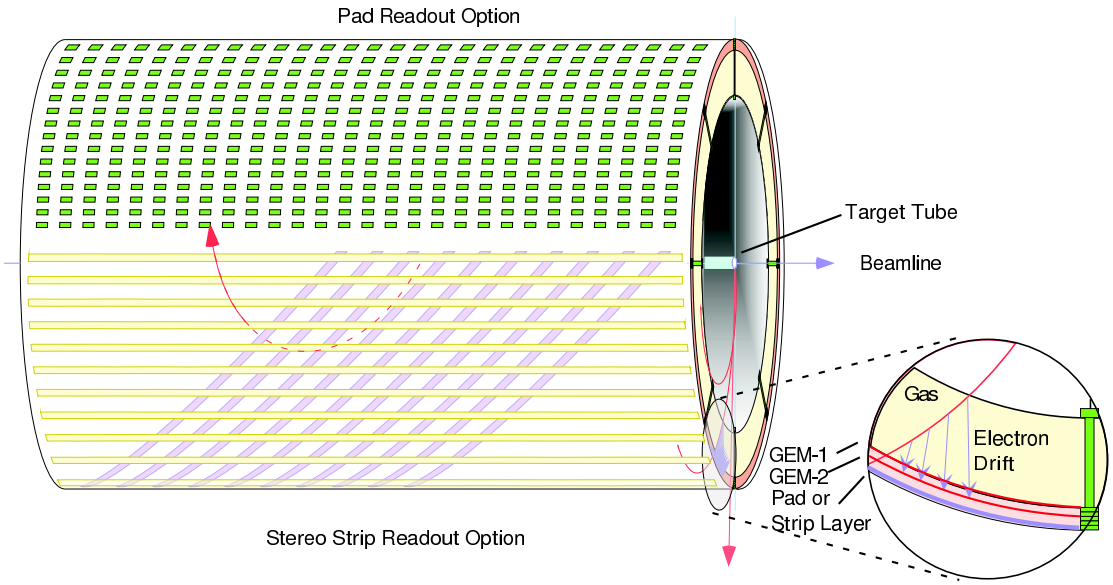

Figure 13: Sketch of the radial time projection chamber for BONUS. In this figure the upper portion shows pad readout while the lower portion shows readout by two planes of strip electrodes providing stereo coordinate measurements.

drift towards the outer cylinder where appropriate electrodes cause avalanche multiplication. The resulting signal is collected on the outer surface by either individual pads or a stereo arrangement of conductive strips. The locations of the pads (strips) provides position information (azimuthal angle ϕ and distance z along the beam direction) for the collected drift electrons, and the times of their arrivals provide a measure of the radius (r) at which they were produced. A string of pads giving signals constitutes multiple position measurements along the particle's track. By recording the amount of charge produced along the track one can estimate dE/dx and thereby constrain the mass of the particle that produced it.

4.4.1 Conventional Time Projection Chambers

The physical processes involved in TPC operation (notably electron drift and diffusion) have been well-understood for many years. In most instances TPCs are cylinders with the electric (drift) field parallel to the axis. This is especially advantageous when the TPC is placed within and parallel to a solenoidal magnetic field ($\mathbf{B}$), since the electrons are constrained to drift along a line of magnetic flux and therefore suffer very little transverse diffusion during their long transit to a readout device on one of the cylinder ends. The readout devices include multiwire proportional counters with cathode pads or strips, micro-strip gas chambers, and gas electron multipliers (GEMs).

TPCs are typically slow devices, owing to the electron drift velocity in most gases (a few cm/μs or less at atmospheric pressure). A 1 m long TPC may require 100 microseconds for complete electron drift. However, the slow drift speed provides fine position resolution. The large number of measurements on each track allows tracks to be recognized and correctly associated with other tracks from the same event even when multiple events occur during

one drift time interval.

4.4.2 Radial TPC for BONUS

For BONUS a modified concept for the TPC is required. Although the BONUS spectator detector will sit in a solenoidal **B** field, the primary function of this field is to curl up Møller electrons, not to enable magnetic spectrometry. As a result, the field we have to deal with is far from uniform. Drift electrons trapped on **B** field lines would follow a long and complicated path towards the endcaps where sensors would normally be placed. Furthermore, even though a TPC for BONUS may be only 20 cm long, the time required for electrons to drift this distance may be too long for the charged particle rate expected in the detector.

A *radial* TPC, however, seems to be a natural match for the BONUS requirements. By drifting radially outward, across the **B**-field lines instead of along them, the electron drift distance is kept short so that understanding the electron trajectories is simplified. Since the drift distance is only 2–3 cm, the drift time is small, on the order of 2 μs or less. Even with a few MHz background, the detector volume would contain charge from fewer than 10 tracks at any given moment. Electrons drifting through the crossed **B** and **E** fields will undergo a net deflection at the *Lorentz angle*, but this is a tractable problem to analyze.

Finally, although a radial TPC is a new concept for a spectator proton detector, it is not a new idea. A much larger version of what is proposed here was investigated by the Hall D collaboration. Diffusion over the long drift path of their detector would have made the position resolution insufficient, however. In the BONUS RTPC, drift distances are short and position resolution of only 1 mm is sufficient and easily achieved. The STAR collaboration at RHIC investigated RTPCs, then built and installed two of them (the Forward Time Projection Chambers, or FTPCs). The pair is used to measure very forward/backward tracks in RHIC's nucleus-nucleus collisions. Each one is 1.2 m long and about 60 cm in diameter, yet provides 1 mm spatial resolution. A reconstructed Au-Au event, demonstrating successful reconstruction of some 500 tracks, is shown in Fig. 14. The detector we propose for BONUS is smaller and simpler, and will directly benefit from the experience at STAR with the FTPC itself, and with the readout electronics used with it.

4.4.3 Preliminary Design

As shown in Fig. 13, the sensitive volume of the BONUS RTPC will be an annulus with inner radius $\simeq$ 4 cm and outer radius $\simeq$ 6 cm. The 20 cm length (shown in the figure) will extend beyond the target in order to provide coverage from 90° to 160° for the entire target. The 4 cm space between the target vessel and the inner cylinder will be filled with helium to minimize the scattering and energy loss of particles before they enter the detector. This space also serves as a dead zone in which Møller electrons can be curled up without affecting any detector elements. The outer radius (the inner radius of the RTPC) may be altered as we proceed with simulation and prototyping studies.

The inner cylinder of the RTPC, which serves both as a gas barrier and as the first drift electrode, will be 50 μm or less kapton plated with 5 μm gold. Outside $\simeq$ 2 cm of sensitive gas (probably 50/50 neon-DME) will be the first of two GEMs. Another $\simeq$ 0.2 cm out will be the second GEM followed by the readout pads or strips $\simeq$ 0.2 cm later. Although

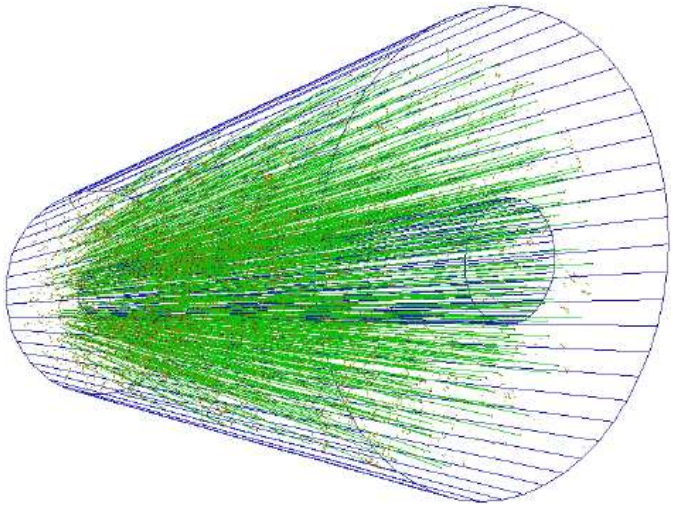

Figure 14: Reconstruction of the Secondary Tracks from a Au-Au Collision in one of the STAR Forward Time Projection Chambers.

each of these four cylindrical electrode assemblies will be largely self-supporting, they will be constrained by precisely machined endcaps and by radial frames spaced periodically in azimuth. The frames will deaden a small and quantifiable part of the chamber volume.

GEMs were chosen as the readout sensors because they are mechanically simple and lend themselves naturally to a curved geometry. A GEM is fabricated by chemically etching closely spaced tiny holes through a kapton sheet clad on both surfaces with a thin layer of copper. A modest voltage (few hundred volts) between the two conductive layers produces a large electric field in the holes. Ionization electrons which enter the holes on the negative-biased side of the GEM initiate a gas avalanche within the holes resulting in a large number of electrons being emitted on the positive side. These secondary electrons can be directed onto a pickup electrode a short distance away, or into another GEM for further amplification. The pickup electrodes collect the resulting charge cloud. Electronics connected to these electrodes sense the charge and record its magnitude and time of arrival.

After significant developments over the last few years [56] under the direction of F. Sauli at CERN, GEMs are now deployed in a number of physics experiments. Notably, a large array of multi-stage GEMs[57] is being used in the COMPASS experiment at the CERN SPS. The BONUS spectator detector would use GEMs wrapped around a cylindrical frame to form a curved surface. Although nobody has used a curved GEM to date, it seems to be a natural extension of the technology and no difficulties are foreseen [58]. Our collaboration with F. Sauli on this detector project will go a long way to ensure that the optimum solution will be found.

The precise geometry of readout electrodes for BONUS is not yet determined. One method which will clearly work is to place an array of regularly spaced pads or short strips distributed uniformly over the surface of the readout cylinder. This is very similar to the readout scheme in use in the STAR FTPC, which instruments 9600 pads in each radial TPC. However, given the smaller size of the BONUS device, it may be possible to collect the charge on two arrays of conductive strips placed on the outer cylinder. Drawing upon technology developed for COMPASS, it is possible to place the two arrays on the inner and outer surfaces of the cylinder at stereo angles to one another and cause them to equally share the amplified charge clusters. This would provide two stereo *views* of the collection cylinder surface, thus providing $\phi - z$ and dE measurements, with a modest number of electronics channels. Concerns over ambiguities due to multiple tracks suggest that pads are the best option, but further analysis and simulation are required before we can determine whether pads or stereo strips are most appropriate for BONUS.

4.4.4 Readout Electronics

The electronics used to read out the RTPC must provide both charge and time information. This problem has been solved for the STAR FTPCs and the main STAR TPC by a system of charge preamplifiers whose output is fed to a switched capacitor array (SCA). The SCA is clocked at 5 MHz, causing the charge collected in each ≈ 200 ns interval to be transported in a bucket-brigade fashion through the chain of capacitors. Upon receipt of a trigger signal, charge stored in the appropriate capacitors is digitized and the results are passed to the data acquisition system. Readout of this system takes about 10 milliseconds. An upgrade is currently planned for the main TPC which will use flash ADCs and digital storage to

significantly reduce the readout time. Such a system has been developed for the ALICE experiment at CERN [59]. A similar (or identical) readout system could be applied to the BONUS RTPC. Discussions about this possibility are currently ongoing with members of the STAR collaboration.

4.5 Cost Estimate

It is estimated that the radial TPC and target will cost less than $270,000, as follows: Our TPC barrel is 20 cm long, with an outer diameter of 13 cm and circumference 40.84 cm. Our pad sizes are projected to be 0.5 cm in z and 0.4 cm (3.5 degrees) in ϕ. We expect, then, to require 40 z pad rows and 103 ϕ pad rows, for a total of 4,120 pads. The Brookhaven STAR TPC electronics cost for everything up to the VME interface was $14.50 per channel in 1997. Assuming an 8% per annum increase to this, we estimate $21.31 per channel for a total RTPC front-end electronics cost of $87,797. We suggest $15,000 for GEM development, and the RTPC mechanics are estimated to cost $50,000. The RTPC and target calibration, gas and cooling systems are estimated to cost $100,000. Finally, the target mechanical design and construction is estimated to cost $15,000, for a total combined cost estimate of $267,797 without contingency. With a 50% contingency, this total will change to $401,695.

We stress that our estimate is based on current design specifications, which may be improved. It is possible to use strip readout, for example. However, we can not think of a probable design change which would cause the cost to rise up significantly from this estimate.

Fabio Sauli has already sent a GEM to Jefferson Lab and, therefore, prototyping can begin immediately. This will allow a clearer breakdown of costs in the near future.

4.6 Alternative Detectors, Silicon

Although the collaboration believes that a radial TPC such as that outlined here would be the best device for accomplishing the goals of this experiment, we note that a cube of silicon strip detectors could be used as well to measure the spectator protons. This detector would have good energy resolution. Timing resolution better than 1 ns could be achieved, allowing for good background rejection for coincidence with scattered electrons. Two layers of silicon detectors are envisioned; the first will be 70 microns thick and the second 500 microns thick. Protons up to 85 MeV/c will stop in the first layer, so tracking will not be possible without knowing the electron vertex. Background rejection will depend on the coincidence timing. Protons above 85 MeV/c will leave a signal in both layers, allowing a rough determination of the vertex. Silicon detectors could handle a rate of 10 kHz/cm^2, and have been used at CERN to withstand 10^{15} protons / cm^2 with a special coating.

Silicon detectors are robust and reliable, and could prove a viable alternative to the radial TPC. Such an alternative, however, would most likely be more expensive. Dead regions would exist for readout and corner areas of such a detector, but the active area could be optimized and dead space is not expected to be a serious problem. A real design effort would be necessary to optimize the detector layout, dimensions, and framing to minimize dead space.

4.7 Engineering Run Request and Experiment Time Line

We request an additional 5 days of engineering beam time prior to the BONUS experiment. This engineering run will allow us to verify a variety of crucial capabilities of the BONUS detector. We need to substantiate the TPC's ability to detect the very important low momentum protons (VIPs), and to detect them in the presence of hadronic background. We need to test the accuracy of our rate predictions, signal to background, and to quantify the use of timing, particle ID, and vertex resolution to accurately measure the outgoing proton associated with the electron event. We can also optimize the magnetic field required, check the coincidence with the electron trigger, establish time and distance calibrations for the TPC, and debug in advance any unforeseen difficulties associated with the commissioning of such a complicated new detector in the experimental environment.

This engineering time will require the solenoid as well as an RTPC prototype, and will therefore be optimally scheduled either directly prior or subsequent to the DVCS experiment E01-113. We need some dedicated time for our target and detector configuration as well.

If the DVCS experiment runs in Spring 2004, this is a reasonable time scale for the engineering run. Should this proposal be approved now, we would have slightly more than a year for TPC and target design and prototyping prior to the engineering run. We believe this time to be more than adequate for prototype development. It is hard to estimate the time required between the engineering run and the full experiment without knowing the engineering results, but we estimate about six months.

5 Expected Results

In this section, we describe the details of our simulation of the proposed BONUS experiment. In particular, we show that we can achieve sufficient resolution in all relevant kinematic variables and adequate statistical and systematic precision for the kinematic bins of interest.

Fortunately, many parameters of relevance (electron acceptance and resolution, reconstruction of proper kinematic variables, singles and coincidence rates) are already well- known from the preliminary analysis of experiment E94-102 ("Inelastic electron scattering off a moving nucleon in deuterium", S. Kuhn and K. Griffioen, spokespersons). This experiment took all of its data in Spring 2002 as part of the E6 run group.

5.1 Preliminary Results from the E6 run period

Experiment E94-102 was proposed to measure scattered electrons in coincidence with emission of a *fast* proton moving backwards relative to the direction of the momentum transfer. The physics motivation for the experiment was to check the validity and limitations of the spectator model, gain information on the modification of the structure function of the neutron due to off-shell effects, and to test the high-momentum part of the wave function of deuterium for exotic components. Since the experiment used the standard CLAS configuration, only recoil protons with momenta above about 250 MeV/c could be reliably detected and reconstructed. Therefore, E94-102 is truly complementary to the present proposal, since the momentum coverage for backward protons begins above the range covered by the experiment proposed here. Data from E94-102 will be extremely valuable to test deviations from

Figure 15: The E6 target cell with plumbing exposed (left) and with heat shields in place (right).

the simple spectator picture assumed for BONUS. Apart from this different emphasis, the two experiments have many common aspects, and therefore the expertise gained in running and analyzing E94-102 is invaluable.

The experiment ran as part of the E6 run group in JLab's Hall B with a 5.75 GeV unpolarized electron beam and an average beam current of 8 nA. The main target was a liquid deuterium cell of 5 cm length (see Fig. 15). This target was developed specifically for E6, with a minimal amount of material in the backward region. The resulting luminosity was close to $L = 1.1 \times 10^{34}\text{cm}^{-2}\text{s}^{-1}$, more than twice what we propose here. The trigger was given by a coincidence between Cherenkov counter (a signal of at least 1 photo-electron) and electromagnetic calorimeter. We also required a track candidate in the sector of the calorimeter hit (Level 2 trigger). The trigger rate for this wide open electron trigger was about 3000 Hz and the deadtime was usually less than 13%. We plan to run with very similar conditions for the proposed experiment, which will yield a comfortably low dead time and data acquisition rate (as well as lower backgrounds) due to the lower luminosity. The open trigger will allow us to scan our data for a wide variety of final states in addition to inclusive electrons.

Data were also taken with a liquid hydrogen target (for the purpose of momentum corrections and cross section normalization) and with an empty target for the purpose of background subtraction. Most of the data were collected with in-bending torus polarity (as proposed here), but E6 also took some exploratory data with electrons bending outward. In 40 calendar days of running the experiment collected a significant amount of data (Table 1) that will be beneficial in conjunction with the data from the proposed experiment.

As of October 2002 the E6 data set was in the stage of preliminary analysis. Based

Target	Magnet Setup	Data Collected (mC)	Data Collected (triggers $\times 10^6$)
Liquid Deuterium (LD_2)	2250 A	9.4855	4055.43
LD_2	-2250 A	0.7793	452.87
Liquid Hydrogen (LH_2)	2250 A	0.6622	209.31
LH_2	-2250 A	0.2436	66.14
Empty (E)	2250 A	2.9387	77.83
E	-2250 A	0.4703	78.51
Total LD_2	-	10.2448	4508.3
Total LH_2	-	0.9058	275.45

Table 1: E6A accumulated statistics

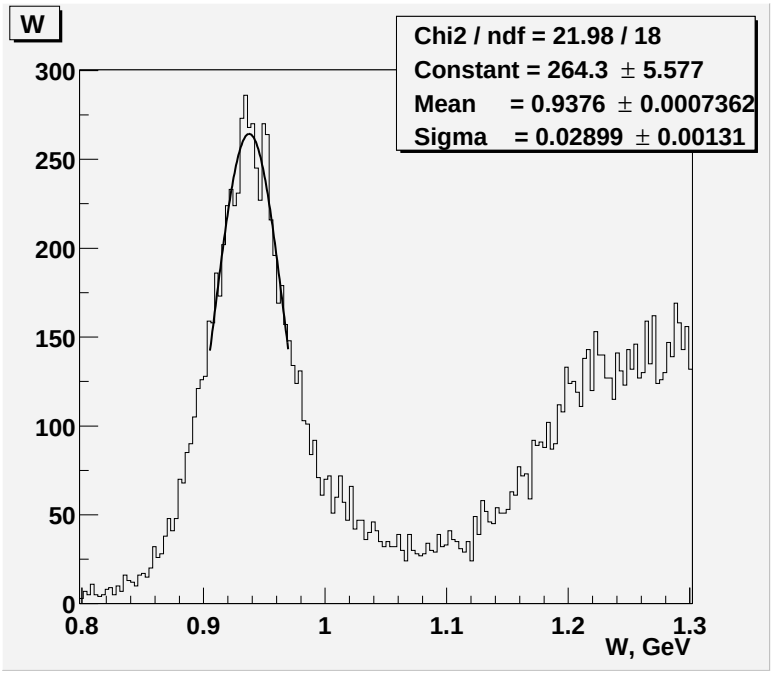

Figure 16: Invariant mass spectrum for the hydrogen target.

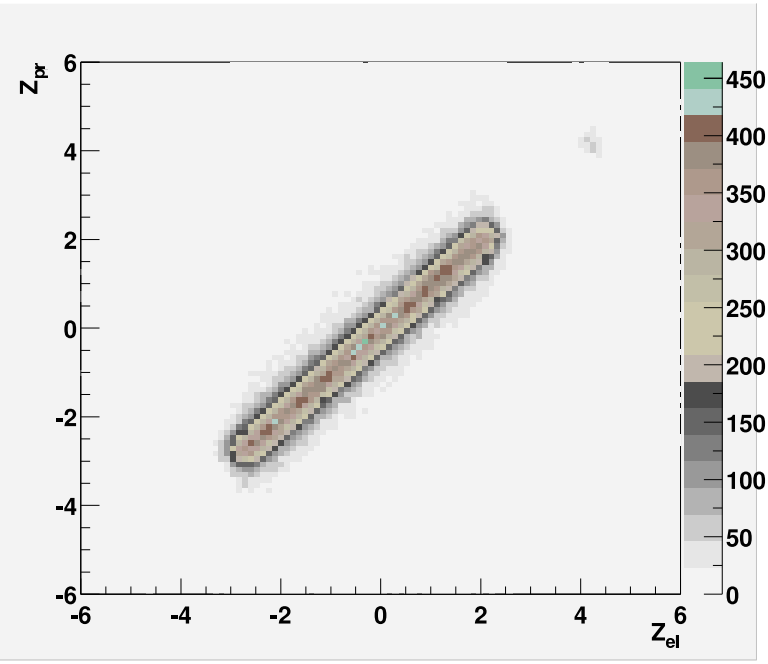

Figure 17: Reconstructed z vertex of the electron vs. that of the proton.

on ≈15% of the deuterium data analyzed with preliminary calibration constants, several quantitative results relevant to this proposal were extracted.

The preliminary analysis provided information on the electron momentum and vertex resolution. The resolution of the elastic peak in the invariant mass spectrum for the hydrogen target after preliminary calibration, angle and momentum corrections was determined to be about 29 MeV (Fig. 16). The standard deviation of the reconstructed z-vertex of the electron was found to be ≈ 1.8 mm (Fig. 17), while that of the proton was about 5 mm due to multiple scattering. The spatial and momentum resolution are similar to what we expect for BONUS.

We developed fiducial cuts in the kinematic variables to exclude regions of CLAS where the trigger and detector efficiency were small or varying rapidly. We also developed a set of electron ID cuts based on the signal height in the Cherenkov counters and the ratio of energy deposited in the electromagnetic calorimeter over momentum. We estimate that the remaining pion contamination for these cuts is at most 2%. We used the same cuts for our simulation of the proposed experiment.

The fiducial cuts determine the kinematic coverage of E6 (Fig. 18a). The electron kinematic coverage will be very similar for the proposed experiment. The statistics accumulated during E6 are sufficient to bin the observables in the kinematic constants of interest (Fig. 18b). The number of reconstructed electrons per trigger is about 3.5% which translates to 100 scattered electrons per second. The rate will be 20 electrons per second at the luminosity of BONUS since we will use a higher torus field (for better resolution) which will reduce the coverage at low Q^2 where the rate is highest.

During E6, roughly 0.24% of all electrons were in coincidence with a backward-moving proton above 250 MeV/c (requiring both an angle above 90° relative to the beam direction and above 110° relative to the $\mathbf{q}$ vector). This result agrees quite well with the coincident

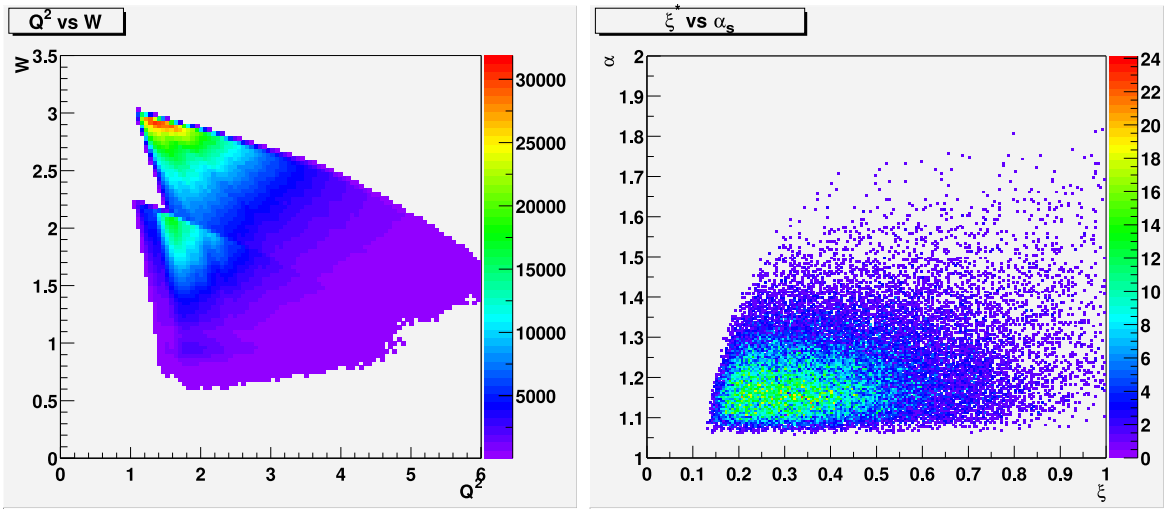

Figure 18: (a) Kinematic coverage in momentum transfer squared (Q^2 in GeV^2) vs. invariant mass (W in GeV) for experiment 94-102. The coverage for the proposed experiment will be very similar. (b) Light-cone fraction of the struck quark (ξ) vs. light-cone fraction of the spectator proton (α) for E6. The coverage for the proposed experiment will be concentrated between $\alpha = 1.0$ and $\alpha = 1.1$.

rate of 0.27% predicted by our simulation for the E6 case, giving us confidence in the reliability of our code. Roughly 2/3 of the measured coincidences were real and 1/3 accidental. The accidental rate can be further suppressed by using timing, energy loss and vertex information on the proton candidate. Based on a coincidence time window of about 20 ns for E6 conditions we estimate that the measured accidental coincidence rate corresponds to a hadronic singles rate of about 0.05 per μs. Since E6 was only sensitive to roughly 5% of the total momentum distribution in deuterium above 60 MeV/c, this translates to a total hadronic rate of 1 MHz above that threshold. Due to the lower luminosity in the proposed experiment, we expect a substantially lower rate of about 0.4 MHz.

As the last step of the preliminary analysis of E6 data, we use the measured backward proton momenta to calculate the invariant final state mass of the struck neutron in the spectator picture. This improved the resolution of the invariant mass of the unobserved final state substantially compared to the case where we calculated it simply assuming the struck neutron to be stationary (see Fig. 19). This is an indication that the kinematic corrections based on the spectator model seem to work well even at the high spectator momenta of E6.

5.2 Monte Carlo Simulation

We developed a Monte Carlo simulation for the proposed experiment to determine expected count rates, kinematic coverage and resolution. The event generator for this simulation uses a parameterization of the world's structure function data on protons and deuterons and a realistic model of the deuteron momentum wave function (based on the Paris potential) to produce both inclusive electron scattering events and electron–backward proton coincident events distributed according to the cross section.

The electron acceptance was determined by using the same fiducial cuts (based on initial

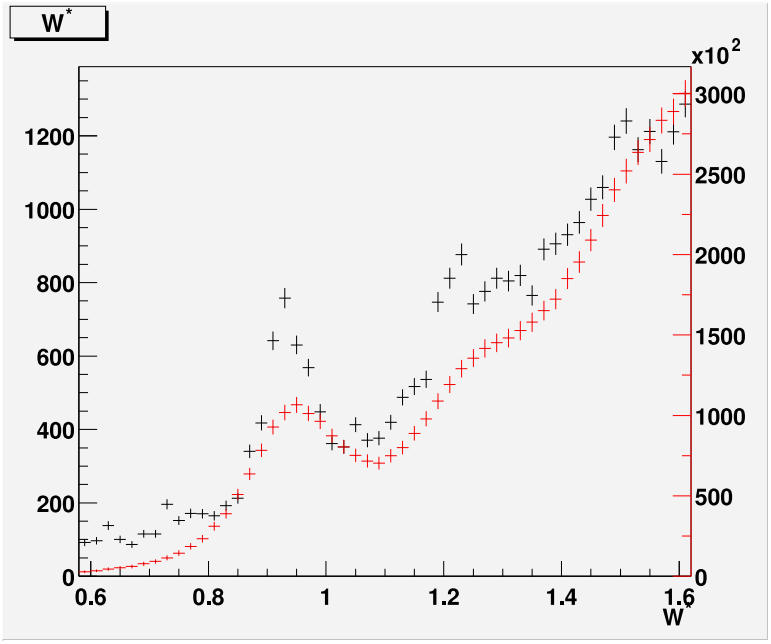

Figure 19: Invariant mass distribution (W in GeV) of the unobserved final state calculated using the spectator momentum to determine the momentum of the struck nucleon [black points] compared to the conventional invariant mass, calculated assuming the struck nucleon is stationary [red points].

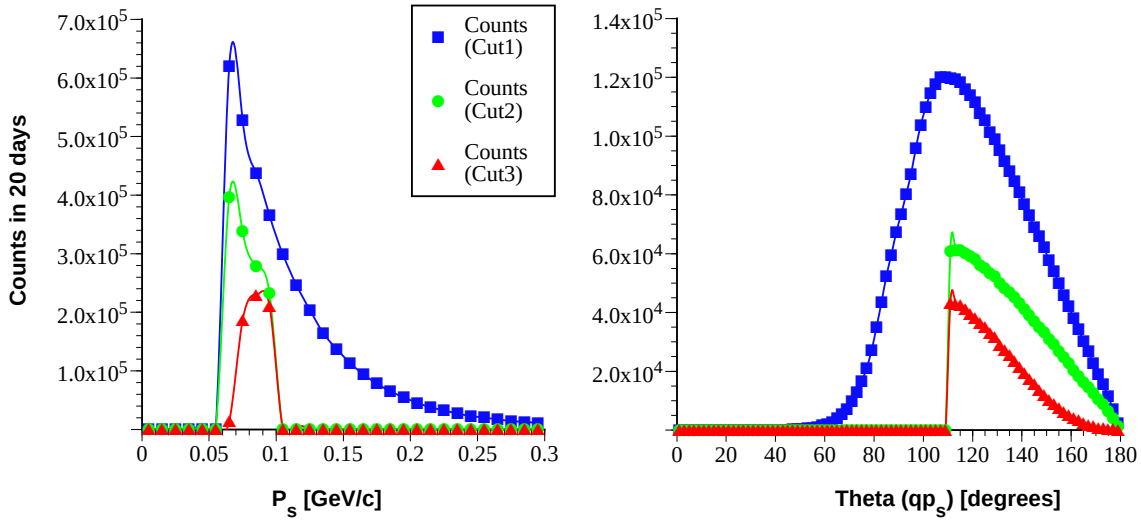

Figure 20: Expected number of counts for the proposed experiment in 20 days of ideal running at 6 GeV, plotted as a function of the spectator momentum p_s (left) and as a function of the angle between the spectator direction and the $\mathbf{q}$ vector, θ_{qp_s} (right). Cut 1 (squares) contains all events where an electron is detected within fiducial cuts and a proton is emitted at more than 60 MeV/c momentum and at more than 90° with respect to the beam direction. Cut 2 (circles) also requires that the spectator momentum is below 100 MeV/c and θ_{qp_s} is more than 110°. The final Cut 3 (triangles) requires that the spectator is detected within the acceptance of the proposed recoil detector.

momentum and direction) as in E6 (see previous subsection). This method avoids time consuming GEANT simulation since the fiducial cuts are well within the region of uniform CLAS acceptance and efficiency. We could show that both inclusive electron rates and electron–proton coincidence rates predicted by our analog simulation of E6 were within 20% of the measured results, which is sufficiently accurate for the present purpose of estimating rates. The electron momentum resolution was taken to be the same as for E6 ($\sigma \approx 29$ MeV in W for the elastic peak) since our running conditions will be very similar (actually better for the proposed experiment due to the smaller rate and higher torus field). The electron vertex was assumed to have a sigma of 2 mm, again the same as measured in E6.

The backward protons above an initial momentum of 60 MeV/c were followed through a simple simulation of the target and recoil detector system. Both energy loss and multiple scattering in all components of the target and detector were taken into account, as well as the curvature of the track in the solenoid field. Protons that penetrated the active region of the detector by at least 1 cm were counted. For the final data sample discussed below, we considered only protons below 100 MeV/c initial momentum and with a scattering angle of more than 90° relative to the beam and more than 110° relative to the direction of the momentum transfer vector. These very important protons (VIPs) correspond to scattering events off nearly on-shell neutrons, with very little uncertainty from final state interactions and off-shell effects (see Section 3). Fig. 20 shows the spectator momentum acceptance of the proposed experiment according to our simulation.

It is important to note that we will be able to separate pions from protons in our RTPC detector up to momenta of at least 200 MeV/c by comparing the track curvature in the solenoid field and the energy loss in the active detector volume. We will thus be able to make a direct connection with the momentum range covered by E6, which will allow us to study in detail the onset of off–shell effects and other deviations from the simple spectator picture and to pin down the extrapolation curve shown in Fig. 11 at the high momentum end.

5.3 Resolution

In the proposed experiment, we will use the track curvature in the solenoid field to separate protons from pions with similar energy deposit (and therefore much lower momentum) in the active detector region. On the other hand, we can use the deposited energy to calculate the initial momentum of the proton (once its identity has been established). With a 25% resolution on the deposited energy, we can achieve a resolution $\Delta p/p = 10\% \times (p/100\,\mathrm{MeV/c})$, more than sufficient for the purpose of kinematic corrections for the initial state motion of the unobserved neutron. We are confident that the proposed TPC will have sub-mm resolution on all track parameters. However, if we assume as a worst–case scenario that the resolution on both the track beginning and track end in the 2 cm active region is determined by the longitudinal pad size, $\sigma_z = 4\ \mathrm{mm}/\sqrt{12}$, we can still extrapolate the proton vertex to about 5 mm resolution, even including multiple scattering. This will yield a suppression of about a factor of 5 for accidental coincidences by requiring the proton and electron vertices to be within 1 cm of each other. Once a proton has been identified as being in true coincidence with a scattered electron, we can use the superior electron vertex reconstruction and the average track position inside the TPC to determine the scattering angle to about 3° to 4°

precision. The resolution in ϕ will be even better due to the narrow beam width and the smaller pad size in that direction.

Taken together, we will resolve the initial backward proton momentum to substantially better than 10 MeV/c and the relative angle between the direction of $\mathbf{q}$ and the proton to about 2°. This results in an additional uncertainty on the reconstructed missing mass W of the unobserved neutron of about 11 MeV at the elastic peak and less than 10 MeV in the resonance region for the 4 GeV run, and about 50% more for 6 GeV. This additional uncertainty is a minor contribution to the overall resolution which is dominated by the electron reconstruction and will be around 20 MeV for 4 GeV and 30 MeV for 6 GeV. Both the light cone momentum α of the spectator proton and the inferred scaling variable x for the struck neutron will be determined to better than 1% precision.

5.4 Background Events

The largest potential source of background events comes from Møller electrons. We will set the magnetic field of the solenoid to curl up the vast majority of these electrons (up to 20 MeV). The remaining higher–momentum Møller electrons will move forward at an angle below 9° and therefore miss the RTPC recoil detector. All Møller electrons will be stopped in the downstream beam collimator. Any remaining electrons will be minimum ionizing and therefore easily distinguished from the slow protons we are interested in.

Low momentum pions could also potentially create a background contribution. They are unlikely to come from high momentum transfer interactions, i.e. they are not likely to be in true coincidence with the scattered electron. Therefore, they can be considered a part of the overall uncorrelated hadron singles rate which we estimated in the subsection on E6. Very low momentum pions will curl up in the solenoid field and not reach the recoil detector. At somewhat higher momenta (above 20 MeV/c), they can deposit a relatively large signal in the drift region of the TPC; however, they will be bent by a large angle in ϕ which can be easily detected using the azimuthal track length in the TPC. At momenta above 30 MeV/c, their energy loss in the active volume will be much smaller (by at least a factor of 3) than that of any of the protons of interest (VIPs).

The background contribution from entrance and exit window of the target can be suppressed by vertex cuts or subtracted using empty target runs. We will also use runs with hydrogen instead of deuterium as target gas to study additional background sources (as well as for calibration purposes).

The most important remaining background will be from accidental coincidences between scattered electrons and unrelated hadrons (pions and protons). Extrapolation from the results from E6 (see Section 5.1) yields a rate of about 400 kHz for these hadrons above 60 MeV/c. About 22% of this rate will be below 100 MeV/c and within the acceptance of our recoil detector. We will be able to discriminate against hadrons which are more than $\pm$100 ns out of time with the electron by extrapolating the arrival time of the drift electrons back to the entrance of the drift region. This yields an overall probability of 1.8% for an accidental hadron to be in time with a detected electron. This number is to be compared with a true coincidence rate of about 2.3%. The accidental rate will be further suppressed by eliminating pions (see above) and by applying a cut of $\pm$1 cm on the difference between proton and electron vertex, yielding a true to accidental ratio of at least 5:1. This background

can be measured by studying out–of–time and vertex–displaced coincidences and by varying the beam current (since the accidental rate varies like the luminosity squared). We can thus subtract the contribution of accidental coincidences from our signal with only slight increase in the statistical error (by about 20%).

5.5 Systematic errors

We need to know the total luminosity to extract cross sections from our data. In addition, uncertainties in the overall acceptance and trigger and cut efficiencies enter the cross section error. Typical experience with previous CLAS experiments show that an overall error of about 5% on extracted cross sections can be achieved. We will use quasi–elastic $d(e,e'p)n$ events (scattering off the proton) as well as elastic scattering off the neutron with spectator proton detection at low Q^2 to normalize our results and thereby minimize this systematic error.

A second systematic error comes from the acceptance and efficiency of our proton recoil detector. We will model the detector and calibrate it using kinematically complete events (e.g., $d(e,e'p_s\pi^-)p$). We estimate another 5% uncertainty from this source. In addition, the extracted cross section on the neutron depends on the integrated probability of the deuteron wave function in momentum space over the acceptance of our detector. The variation from different microscopic models of the deuteron for that probability to find a proton above our threshold of about 60 MeV/c is less than 1%.

The combined uncertainty from the sources discussed so far is about 7%. However, we can reduce this uncertainty substantially by normalizing our results for the neutron structure function F_2^n at low x (high W) to existing data from inclusive electron scattering on deuterium. In this region, the correction for nuclear effects is small. We estimate a remaining error of less than 3% on the combined effects discussed above.

Additional theoretical errors come from deviations from the simple spectator picture, like breaking of factorization (less than 1%), remaining off-shell effects (up to 2% uncertainty) and final state interaction (3% to 5%) (see Section 3.). We can study these effects by subdividing our data into several bins of spectator momentum and also by comparing with the results from E6. Using the extrapolation method outlined towards the end of Section 3, we will be able to reduce the overall theoretical error to the order of 3%.

We estimate our overall systematic uncertainty on the extracted cross sections to be 9% at the highest values of x. Normalizing our data at low x (high W) as outlined above will reduce that systematic error to about 5% from point to point.

Extraction of the structure function F_2 from the measured cross section requires knowledge of the longitudinal to transverse cross section ratio, R. This experiment will not be capable of extracting both F_2 and R simultaneously, and will therefore have to make assumptions for the latter. This is not an uncommon practice for JLab experiments, and was estimated to introduce a 2% uncertainty on F_2 extractions from inclusive electron-proton scattering in the resonance region [13]. However, precision measurements of R on hydrogen in the resonance region from $0.5 \leq \mathrm{Q}^2 \leq 4.5$ GeV^2 have recently become available [60], and an experiment has been approved to measure R to high precision, covering this same kinematic regime, using a deuterium target (JLab Experiment E02-109). These new measurements may allow for an even smaller systematic uncertainty in the proposed extractions

of F_2 on the neutron, since previous estimates used exaggerated extrapolations from deep inelastic scattering.

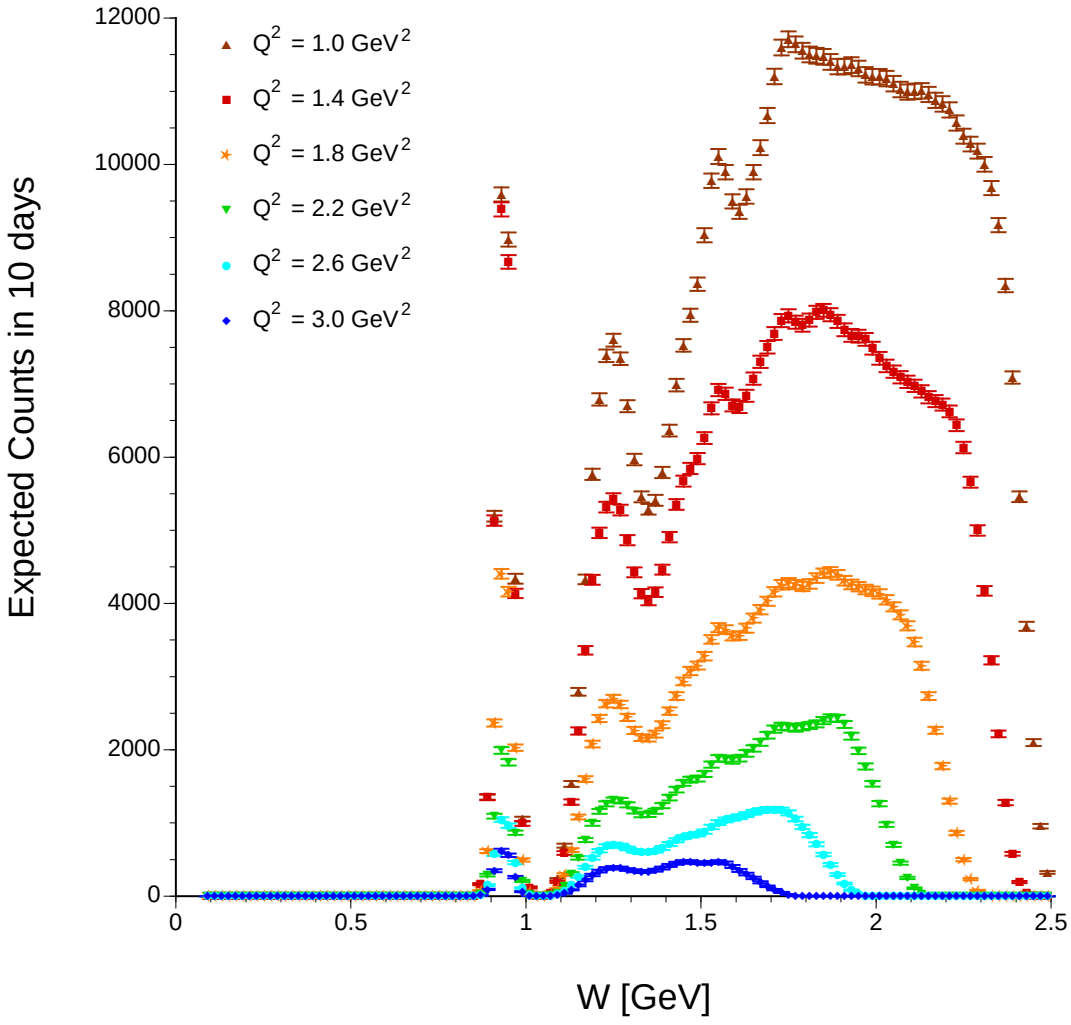

Figure 21: Expected number of counts for the proposed experiment in 10 days of ideal running at 4 GeV, plotted as a function of the reconstructed mass W of the (unobserved) final state. The data sets are for different four-momentum transfer Q^2.

5.6 Expected Accuracy

We propose to collect 10 days (100% efficiency) of data on deuterium with 4 GeV beam and another 20 days with 6 GeV. The 10 cm long target filled with 7.5 atm deuterium gas at room temperature and the 200 nA electron beam will yield a combined luminosity of about 4×10^{33} cm^{-2}s^{-1}.

Our simulation shows that under these conditions, we will collect a total of 2 M events with coincident detection of recoil protons below 100 MeV/c and above 110° relative to the **q** vector (VIPs) at 4 GeV, and another 840,000 events at 6 GeV. The average spectator light

cone fraction will be $\alpha = 1.08$. We will cover a range in W from the elastic peak to about $W = 3.2$ GeV and Q^2 from 1 to 5 GeV^2.

In Fig. 21, we show the expected number of coincident events of the type $d(e, e'p_s)X$, for several bins in Q^2 and 4 GeV beam energy. The expected results are tabulated in Table 2. Similarly, our expected results for 20 days of 6 GeV running are shown in Table 3. Clearly, we will collect ample statistics to study F_2^n in the resonance region and beyond, and to further subdivide the data into bins of recoil momentum to study the approach towards the on–shell neutron point.

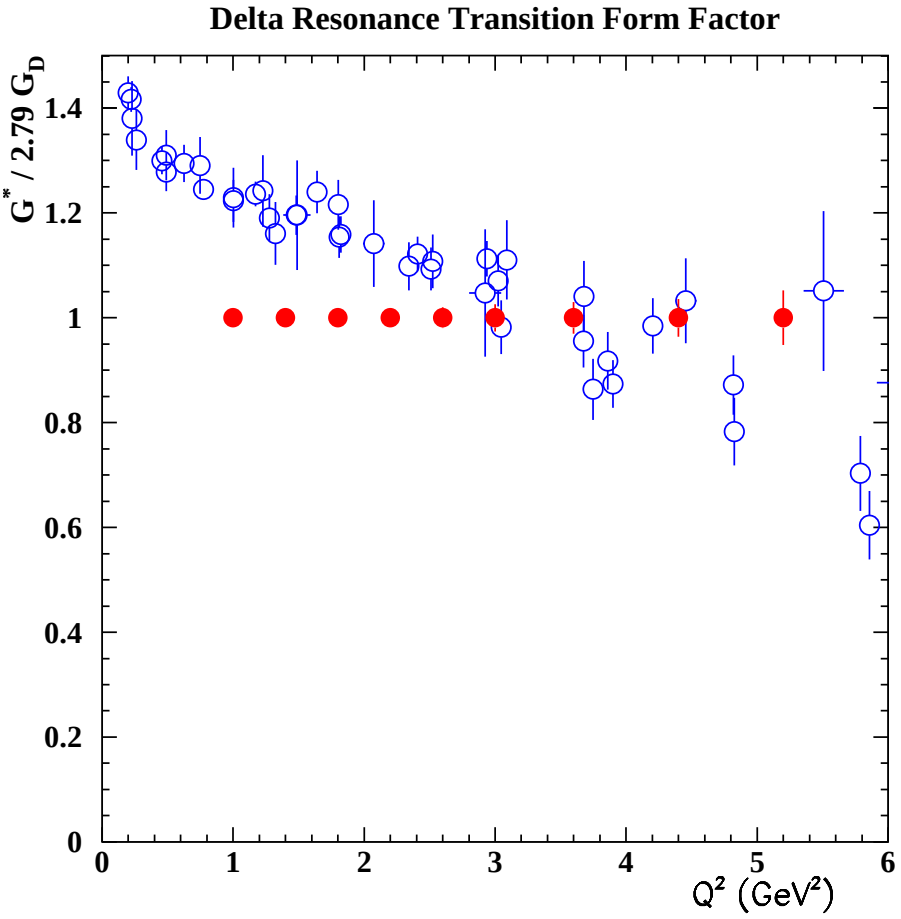

Figure 22: Projections for the $n \to \Delta^\circ$ transition form factor as extracted from an inclusive $d(e, e'p_s)$ reaction (solid circles). Statistical uncertainties only are shown. For comparison, the results for the $p \to \Delta^+$ transition form factor as extracted from inclusive $p(e, e')$ data from SLAC and DESY are shown (open circles), with total uncertainties [61].

Fig. 22 highlights the statistical precision of a possible extraction of the magnetic form factor G_M^* for the $n \to \Delta^\circ$ transition from these inclusive $n(e, e')$ data. Systematic uncertainties are expected to be 5-6%, comparable to the statistical precision for the higher Q^2 projected data points. The projected data points (solid circles) are arbitrarily shown to scale with the dipole form factor, G_D, although the SLAC data agree with a fall off of this form

factor with Q^2 similar to the $p - \Delta$ transition. For comparison, the proton data are also shown.

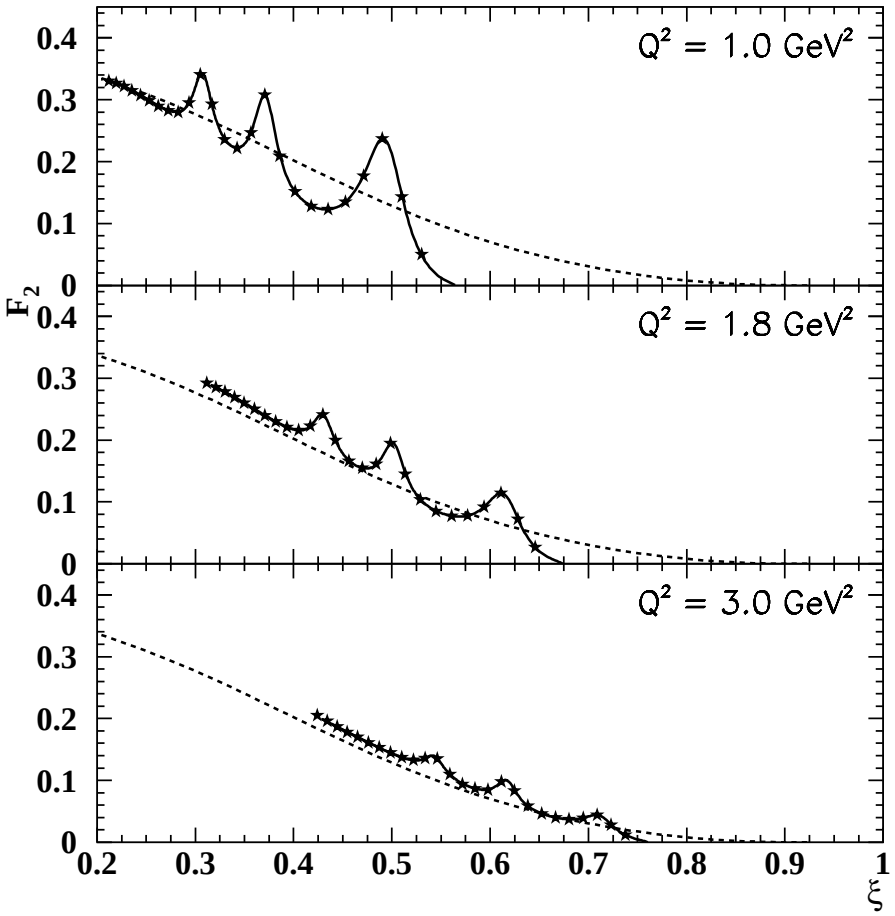

Figure 23: Sample neutron F_2 structure function spectra at $Q^2 = 1.0$, 1.8 and 3.0 GeV^2, plotted as a function of the Nachtmann scaling variable ξ. Since the neutron structure function in the resonance region is unknown, the curves depict a parameterization of proton resonance region data (solid curve) and the NMC fit of deep inelastic structure function data at $Q^2 = 10$ GeV^2 (dashed curve). The statistical uncertainty is smaller than the symbols, and is typically 0.6%, 1%, and 2-3%, at $Q^2 = 1.0$, 1.8, and 3.0 GeV^2, respectively.

The data we plan to collect will also allow for quark–hadron duality studies in the neutron resonance region with very good precision. To illustrate this, Fig. 23 shows a sample neutron F_2 structure function spectra at three values of Q^2, as a function of the Nachtmann scaling variable $\xi = 2x/[1 + \sqrt{1 + 4m^2x^2/Q^2}]$. Since no precise neutron resonance transition model exists yet, we actually plot the results of the existing proton resonance model, at $Q^2 = 1.0$, 1.8, and 3.0 GeV^2 (top to bottom). The dashed curve is from a parameterization of deep inelastic proton structure function data at $Q^2 = 10$ GeV^2.

Although the neutron resonance structure function and deep inelastic structure function data and parameterizations will obviously differ from the proton, we believe this is a good

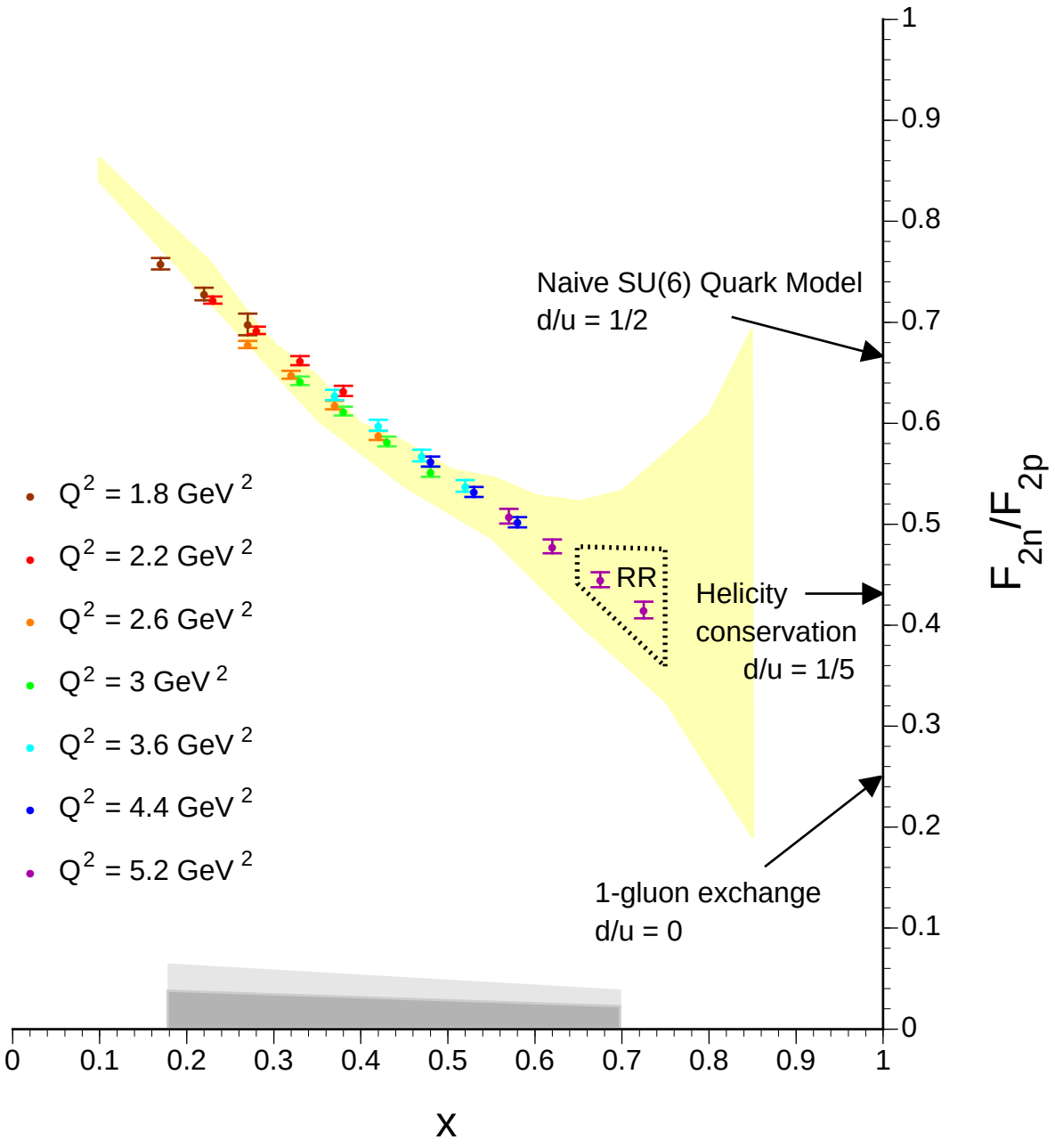

Figure 24: Ratio F_2^n/F_2^p versus x. The small data points indicate the expected results of the proposed experiment for several different bins in Q^2 with statistical error bars. (The simulated data for different Q^2 bins were drawn slightly offset from each other). Estimated systematic errors due to experimental and theoretical uncertainties are indicated by the band at the bottom (light shade for total systematic error, heavy shade for point-to-point error after normalization at low x). The arrows indicate the different possible approaches to the limit $x \to 1$ discussed in Section 3. The shaded area indicates the range of uncertainty from existing data due to different treatment of nuclear effects (see Fig. 3).

example of the potential quality of the neutron data attainable with BONUS. The projected data encompasses running at both 4 and 6 GeV. Typical statistical uncertainties are between 1 and 3%. To investigate variations in local duality from resonance to resonance region this statistics will be quite sufficient.

Our 6 GeV data will allow us to expand substantially the range in x over which the neutron structure function F_2^n is known with good statistical precision and with small theoretical uncertainties. Fig. 24 shows the statistical precision we can achieve for the ratio F_2^n/F_2^p as a function of x, for several bins in Q^2. The lightly shaded band on the x–axis indicates our estimate of the total systematic error, from the combined experimental (acceptance, efficiency, event reconstruction, luminosity) and theoretical (deuteron wave function, off-shell and final state interaction effects) uncertainties. By normalizing our data to the well-known (and unambiguous) data at low x, we can extract the high–x behavior with much smaller uncertainty indicated by the heavy shaded band.

The highest point in x which is still in the deep inelastic region $W \geq 2$ GeV is at $x = 0.625$, clearly in a region where valence quarks are dominant and existing data begin to become uncertain because of nuclear effects (indicated by the shaded area). If we extend these data to include $W \geq 1.5$ GeV, we can add two more points in x as indicated with the shaded region labeled "RR" ("Resonance Region") in Fig. 24. At these high values of Q^2 (≈ 5 GeV^2) and W, it is likely that duality is a very good approximation and we can interpret our results directly in terms of the ratio of d/u valence quark distributions. Of course, we will be able to test duality up to $x = 0.6$ over the whole range of Q^2 and W using our own data. Clearly, the high precision data set indicated in Fig. 24 will allow a comprehensive study of the x and Q^2 dependence of the structure function F_2^n in the valence region, for the first time unclouded by uncertainties from nuclear binding effects.

Finally, we will also be able to contribute significantly to the world's data set on elastic neutron form factors. The expected statistical and systematic errors for each measured Q^2 and $W = M_n$ are listed in Tables 2 and 3 as well. The statistical errors range from 0.5% at $Q^2 = 1$ GeV^2 to 5% at our kinematic limit, $Q^2 = 5$ GeV^2. The systematic errors will be of order 6%. We can normalize our results at small Q^2, where good precision data are available, and can extract the elastic cross section with good accuracy at the higher Q^2. This will allow us to determine the absolute magnitude of the form factor G_M^n with a largely independent method and comparable uncertainty as the dedicated experiment E94-017 (E5 run group in CLAS).

6 Summary and Beam Time Request

We propose the construction of a thin gas target and a radial time projection chamber (RTPC) detector for measuring recoiling protons or light nuclei in CLAS. Such a detector paves the way for a new class of experiments on atomic nuclei at Jefferson Lab.

By tagging the electron scattering from a nucleon with the nuclear remnants, we can measure the nucleon's motion before scattering and control how far off shell it is. This is especially important at high x where Fermi-motion effects in inclusive measurements are substantial. Essential for such measurements is the experimental requirement to observe the smallest possible recoil momenta for the nuclear remnants. With the proposed RTPC

Q^2 [GeV^2]	x	W [GeV]	E' [GeV]	θ_e [°]	Rel. stat. err.	Rel. syst. err.
1	0.175	2.366	0.957	29.6	0.003	0.051
1	0.225	2.08	1.633	22.6	0.002	0.051
1	0.275	1.876	2.064	20	0.003	0.052
1	0.325	1.72	2.362	18.7	0.003	0.052
1	0.375	1.596	2.58	17.9	0.004	0.052
1	0.425	1.495	2.747	17.4	0.004	0.053
1	0.475	1.41	2.879	16.9	0.006	0.053
1	0.525	1.337	2.986	16.6	0.006	0.054
1	0.575	1.273	3.074	16.4	0.006	0.054
1	0.625	1.217	3.148	16.2	0.007	0.055
1	0.675	1.168	3.211	16	0.009	0.055
1	0.725	1.123	3.266	15.9	0.018	0.056
1	0.775	1.083	3.313	15.8	0.078	0.056
1	1	0.939	3.468	15.4	0.005	0.06
1.4	0.225	2.388	0.687	41.8	0.005	0.051
1.4	0.275	2.138	1.289	30.2	0.003	0.052
1.4	0.325	1.947	1.706	26.2	0.003	0.052
1.4	0.375	1.793	2.012	24.1	0.004	0.052
1.4	0.425	1.666	2.246	22.8	0.004	0.053
1.4	0.475	1.559	2.431	21.9	0.005	0.053
1.4	0.525	1.466	2.58	21.2	0.006	0.054
1.4	0.575	1.384	2.704	20.7	0.007	0.054
1.4	0.625	1.312	2.807	20.3	0.007	0.055
1.4	0.675	1.247	2.896	20	0.007	0.055
1.4	0.725	1.189	2.972	19.8	0.009	0.056
1.4	0.775	1.135	3.038	19.5	0.017	0.056
1.4	0.825	1.086	3.096	19.4	0.089	0.057
1.4	1	0.939	3.255	18.9	0.005	0.06

Table 2: Expected relative statistical and point–to–point systematic error on each data point within the kinematic coverage with 4 GeV beam energy. (Continued next page.)

Table 2 continued:

Q^2 [GeV^2]	x	W [GeV]	E' [GeV]	θ_e [°]	Rel. stat. err.	Rel. syst. err.
1.8	0.325	2.149	1.051	38.2	0.006	0.052
1.8	0.375	1.97	1.444	32.4	0.005	0.052
1.8	0.425	1.821	1.745	29.4	0.005	0.053
1.8	0.475	1.694	1.982	27.6	0.006	0.053
1.8	0.525	1.584	2.174	26.3	0.007	0.054
1.8	0.575	1.487	2.333	25.4	0.007	0.054
1.8	0.625	1.401	2.466	24.7	0.009	0.055
1.8	0.675	1.322	2.58	24.1	0.01	0.055
1.8	0.725	1.251	2.678	23.7	0.009	0.056
1.8	0.775	1.185	2.763	23.3	0.012	0.056
1.8	0.825	1.124	2.838	23	0.028	0.057
1.8	1	0.939	3.042	22.2	0.007	0.06
2.2	0.375	2.133	0.876	46.7	0.015	0.052
2.2	0.425	1.964	1.244	38.8	0.008	0.053
2.2	0.475	1.82	1.534	34.8	0.007	0.053
2.2	0.525	1.695	1.769	32.4	0.008	0.054
2.2	0.575	1.584	1.963	30.7	0.009	0.054
2.2	0.625	1.484	2.126	29.5	0.01	0.055
2.2	0.675	1.393	2.265	28.5	0.012	0.055
2.2	0.725	1.31	2.384	27.8	0.013	0.056
2.2	0.775	1.233	2.488	27.2	0.013	0.056
2.2	0.825	1.161	2.58	26.7	0.02	0.057
2.2	1	0.939	2.829	25.5	0.011	0.06
2.6	0.475	1.938	1.085	45.5	0.02	0.053
2.6	0.525	1.798	1.363	40.4	0.012	0.054
2.6	0.575	1.674	1.592	37.3	0.011	0.054
2.6	0.625	1.563	1.785	35.1	0.012	0.055
2.6	0.675	1.461	1.949	33.6	0.014	0.055
2.6	0.725	1.367	2.09	32.4	0.017	0.056
2.6	0.775	1.279	2.214	31.4	0.016	0.056
2.6	0.825	1.197	2.322	30.7	0.019	0.057
2.6	0.875	1.119	2.418	30.1	0.05	0.058
2.6	1	0.939	2.616	28.9	0.015	0.06
3	0.575	1.76	1.222	46.1	0.042	0.054
3	0.625	1.638	1.444	42.2	0.021	0.055
3	0.675	1.525	1.633	39.6	0.018	0.055
3	0.725	1.421	1.797	37.7	0.019	0.056
3	0.775	1.324	1.939	36.2	0.022	0.056
3	0.825	1.232	2.064	35.1	0.022	0.057
3	0.875	1.145	2.174	34.2	0.041	0.058
3	1	0.939	2.403	32.4	0.021	0.06

Q^2 [GeV^2]	x	W [GeV]	E' [GeV]	θ_e [°]	Rel. stat. err.	Rel. syst. err.
1.4	0.175	2.735	1.74	21.1	0.007	0.051
1.4	0.225	2.388	2.687	16.9	0.007	0.051
1.4	0.275	2.138	3.289	15.3	0.013	0.052
1.4	0.325	1.947	3.706	14.4	0.031	0.052
1.8	0.225	2.661	1.74	24	0.004	0.051
1.8	0.275	2.372	2.515	19.9	0.005	0.052
1.8	0.325	2.149	3.051	18	0.006	0.052
1.8	0.375	1.97	3.444	17	0.007	0.052
1.8	0.425	1.821	3.745	16.3	0.009	0.053
1.8	0.475	1.694	3.982	15.8	0.011	0.053
1.8	0.525	1.584	4.174	15.4	0.014	0.054
1.8	0.575	1.487	4.333	15.1	0.017	0.054
1.8	0.625	1.401	4.466	14.9	0.022	0.055
1.8	0.675	1.322	4.58	14.7	0.03	0.055
1.8	0.725	1.251	4.678	14.5	0.034	0.056
1.8	0.775	1.185	4.763	14.4	0.039	0.056
1.8	0.825	1.124	4.838	14.3	0.078	0.057
1.8	1	0.939	5.042	14	0.05	0.06
2.2	0.275	2.585	1.74	26.5	0.005	0.052
2.2	0.325	2.335	2.396	22.6	0.005	0.052
2.2	0.375	2.133	2.876	20.6	0.006	0.052
2.2	0.425	1.964	3.244	19.4	0.007	0.053
2.2	0.475	1.82	3.534	18.5	0.008	0.053
2.2	0.525	1.695	3.769	17.9	0.009	0.054
2.2	0.575	1.584	3.963	17.5	0.011	0.054
2.2	0.625	1.484	4.126	17.1	0.012	0.055
2.2	0.675	1.393	4.265	16.9	0.015	0.055
2.2	0.725	1.31	4.384	16.6	0.017	0.056
2.2	0.775	1.233	4.488	16.4	0.017	0.056
2.2	0.825	1.161	4.58	16.3	0.025	0.057
2.2	0.875	1.094	4.661	16.1	0.12	0.058
2.2	1	0.939	4.829	15.8	0.016	0.06
2.6	0.325	2.506	1.74	28.9	0.006	0.052
2.6	0.375	2.284	2.308	25	0.006	0.052
2.6	0.425	2.097	2.742	22.9	0.007	0.053
2.6	0.475	1.938	3.085	21.6	0.008	0.053
2.6	0.525	1.798	3.363	20.7	0.009	0.054
2.6	0.575	1.674	3.592	20	0.01	0.054
2.6	0.625	1.563	3.785	19.5	0.012	0.055
2.6	0.675	1.461	3.949	19.1	0.014	0.055
2.6	0.725	1.367	4.09	18.7	0.018	0.056
2.6	0.775	1.279	4.214	18.5	0.018	0.056
2.6	0.825	1.197	4.322	18.2	0.02	0.057
2.6	0.875	1.119	4.418	18	0.055	0.058
2.6	1	0.939	4.616	17.6	0.018	0.06

Table 3: Expected relative statistical and point–to–point systematic error on each data point

Table 3 continued:

Q^2 [GeV^2]	x	W [GeV]	E' [GeV]	θ_e [°]	Rel. stat. err.	Rel. syst. err.
3	0.325	2.667	1.085	39.7	0.011	0.052
3	0.375	2.425	1.74	31.1	0.007	0.052
3	0.425	2.223	2.241	27.3	0.008	0.053
3	0.475	2.049	2.637	25.2	0.009	0.053
3	0.525	1.896	2.957	23.7	0.01	0.054
3	0.575	1.76	3.222	22.7	0.011	0.054
3	0.625	1.638	3.444	22	0.013	0.055
3	0.675	1.525	3.633	21.4	0.015	0.055
3	0.725	1.421	3.797	20.9	0.018	0.056
3	0.775	1.324	3.939	20.5	0.021	0.056
3	0.825	1.232	4.064	20.2	0.021	0.057
3	0.875	1.145	4.174	19.9	0.04	0.058
3	1	0.939	4.403	19.4	0.018	0.06
3.6	0.425	2.398	1.49	37	0.008	0.053
3.6	0.475	2.205	1.964	32.1	0.008	0.053
3.6	0.525	2.034	2.349	29.3	0.008	0.054
3.6	0.575	1.882	2.666	27.4	0.009	0.054
3.6	0.625	1.744	2.933	26.1	0.01	0.055
3.6	0.675	1.617	3.16	25.2	0.012	0.055
3.6	0.725	1.499	3.356	24.4	0.015	0.056
3.6	0.775	1.388	3.527	23.8	0.017	0.056
3.6	0.825	1.283	3.676	23.3	0.018	0.057
3.6	0.875	1.182	3.809	22.9	0.025	0.058
3.6	0.925	1.083	3.928	22.5	0.132	0.059
3.6	1	0.939	4.083	22.1	0.021	0.06
4.4	0.525	2.205	1.537	40.4	0.015	0.054
4.4	0.575	2.033	1.925	35.9	0.013	0.054
4.4	0.625	1.877	2.251	33.2	0.012	0.055
4.4	0.675	1.732	2.529	31.2	0.014	0.055
4.4	0.725	1.597	2.768	29.8	0.017	0.056
4.4	0.775	1.469	2.977	28.7	0.02	0.056
4.4	0.825	1.347	3.16	27.9	0.027	0.057
4.4	0.875	1.229	3.322	27.2	0.028	0.058
4.4	0.925	1.113	3.467	26.6	0.077	0.059
4.4	1	0.939	3.657	25.9	0.033	0.06
5.2	0.625	2	1.57	43.6	0.029	0.055
5.2	0.675	1.84	1.898	39.5	0.022	0.055
5.2	0.725	1.689	2.181	36.7	0.022	0.056
5.2	0.775	1.546	2.427	34.8	0.025	0.056
5.2	0.825	1.409	2.644	33.3	0.031	0.057
5.2	0.875	1.275	2.836	32.1	0.036	0.058
5.2	0.925	1.142	3.007	31.1	0.078	0.059
5.2	1	0.939	3.231	30	0.051	0.06

detector, this limit is below 70 MeV/c for protons.

In the case of deuterium, a low-momentum recoiling proton insures that off-shell effects on the neutron are small and we can accurately correct the kinematics for a moving neutron. In the present proposal we concentrate on the resonance and deep-inelastic F_2^n structure function of the neutron for 6 and 4 GeV electron beams in CLAS.

With these data, we can study the Q^2 evolution of the neutron resonances. Unlike for a proton target, neutron resonances are blurred considerably by Fermi motion of nucleons in deuterium. The tagging process will restore the resonance widths to their intrinsic values, and facilitate a better analysis of resonance strength distributed over the range $1 < W < 2$ GeV.

Comparing the data from the deep inelastic region with those from the resonance region, we can test duality for the neutron. Neutron data are essential in order to determine the dynamical origin of duality, and the data that will be collected in this experiment will be of comparable quality to those from earlier experiments in Hall C on the proton.

The deep-inelastic data extend to x as high as 0.625, allowing for an extraction of the ratio F_2^n/F_2^p. This measurement can be extended to 11 GeV which would provide coverage up to $x = 0.85$ in the deep inelastic region. Furthermore, insofar as duality holds for the nucleon resonance region, the F_2^n/F_2^p ratios can be extended to even higher values of x.

The proposed experiment with the low-momentum recoil detector nicely complements the data of the E6 run period in which recoil protons were detected in CLAS for reactions on deuterium. In this case, the minimum proton momentum was about 250 MeV/c. Thus, there is already experience and data for high recoil momenta.

The recoil detector provides a unique opportunity to study any exclusive reaction on the neutron that heretofore was clouded by Fermi motion or by the uncertainty of whether a neutron or proton was struck in the reaction. Since our proposed set up can be used with any of a number of gases as target material, one can envision future experiments with ^{3}He, ^{4}He, Ar, Xe, etc. For example, for an accurate determination of F_2^n/F_2^p, one could use a ^{4}He target, alternately tagging on ^{3}He recoils (a struck neutron) and ^{3}H recoils (a struck proton), thus forming the ratio in a single experiment with small systematic errors. Since both recoiling nuclei are charged, they are both detectable in the RTPC.

The proposed apparatus is also appropriate for low-t coherent vector meson production experiments, in which the nucleus in question must remain in its ground state. It can also be used to measure the decay products of a large nucleus that is highly excited following deep-inelastic scattering, since at JLab energies the struck quark should begin to hadronize within the nuclear volume. Other possible applications include scattering of a virtual "cloud" pion tagged by a backward proton, with hydrogen as target.

This rich program is augmented and extended by higher beam energies. Therefore, measurements now at 6 GeV provide a tantalizing view of what is possible with the 11 GeV upgrade. The RTPC proposed here (without modification) will become part of the experimental equipment for the upgraded CLAS++ detector.

Our group is committed to designing, developing, prototyping and building this unique apparatus. While we are interested in many of the possible extensions listed above, at the present time we specifically request 40 days of new beam time in Hall B for the program of neutron structure measurements described in this proposal, which will make optimum use of this new device.

We request 10 days of 4 GeV beam and 20 more days at 6 GeV. As demonstrated in the previous section, this will allow us to collect high precision data on the neutron, with good statistics, resolution and kinematic coverage, and with minimal uncertainties due to nuclear binding effects. The beam time request was optimized to guarantee that the measurement is not statistics-limited. In addition, the statistical errors listed in the previous section assume that the whole data set for spectator momenta from 70 to 100 MeV/c will be integrated over. For most bins, the statistical precision will be good enough to allow us to study the dependence of the extracted structure functions on the spectator variables (momentum p_s, light cone fraction α and angle relative to the $\mathbf{q}$ vector). We will be able to extrapolate the results measured at low to intermediate off-shellness of the neutron to the on-shell point, as outlined in Section 3.

In addition to the 30 days of data taking on deuterium, we require 5 days of commissioning, calibration and background runs, split between these two energies and directly in conjunction with the main data runs. We will run for about 2 days on a hydrogen target to calibrate all detector elements, and we will take about 2 days worth of empty target runs to subtract backgrounds. We also will need to do some systematic studies to optimize triggers, solenoid field and beam current.

We request 5 more days for a dedicated "engineering run" to check out and commission the new RTPC detector. Ideally, this run would occur well ahead of the main experiment, possibly in conjunction with the commissioning of the DVCS set up in Hall B (since we will be using the same solenoid). Our goal would be to ascertain background rates, resolution, particle identification and other operational parameters of the RTPC or some prototype, to optimize the final setup and prepare the data taking run.

Finally, we request resources from JLab to acquire all needed hardware and to support JLab staff working on this project. We estimate that a calendar month of setup time in the Hall will be needed each time for set up and decomissioning of the target–detector system, including check-out without beam. This time can be shortened considerably if a run is scheduled in conjunction with another experiment using the DVCS solenoid. In this case, about 2 weeks calendar time will be needed to remove the standard CLAS target and to install the RTPC and target system.

References

[1] S. Capstick and W. Roberts, nucl-th/0008028, to appear in Prog. Part. Nucl. Phys.

[2] L. Stuart *et al.*, Phys. Rev. D **58**, 032003 (1998).

[3] L.W. Whitlow *et al.*, Phys. Lett. **B282**, 475 (1992).

[4] P. Amaudruz *et al.*, Phys. Lett. **B295**, 159 (1992).

[5] C.E. Carlson and N.C. Mukhopadhyay, Phys. Rev. D **58**, 094029 (1998).

[6] S. Rock *et al.*, Phys. Rev. D **46**, 24 (1992).

[7] M. Kobberling *et al.*, Nucl. Phys. **B82**, 201 (1974).

[8] P. Stoler, Phys. Rep. **226**, 103 (1993).

[9] P. Stoler, Phys. Rev. Lett. **66**, 1003 (1991).

[10] P. Stoler, Phys. Rev. D **44**, 73 (1991).

[11] C. Keppel, *Proceedings of the Workshop on CEBAF at Higher Energies*, eds. N. Isgur and P. Stoler, 237 (April 1994).

[12] M. Warns *et al.*, Phys. Rev. D **42**, 2215 (1990).

[13] I. Niculescu *et al.*, Phys. Rev. Lett. **85**,1186 (2000); I. Niculescu *et al.*, Phys. Rev. Lett. **85**, 1182 (2000); R. Ent, C.E. Keppel, and I. Niculescu, Phys. Rev. D **62**, 073008 (2000); S. Liuti, R. Ent, C.E. Keppel and I. Niculescu, hep-ph/0111063.

[14] M.E. Christy *et al.* (E94110 Collaboration), *in preparation.*

[15] J. Arrington, J. Crowder, R. Ent, C.E. Keppel, and I. Niculescu, *in preparation*; J. Arrington *et al.* Phys. Rev. C **64**, 014602 (2001).

[16] A. Airapetian *et al.* (HERMES Collaboration), hep-ex/0209018.

[17] N. Isgur, S. Jeschonnek, W. Melnitchouk and J.W. Van Orden, Phys. Rev. D **65**, 054005 (2001); S. Jeschonnek and J.W. Van Orden, Phys. Rev. D **65**, 094038 (2002); V.V. Davidovsky and B.V. Struminsky, hep-ph/0205130; G. Ricco, M. Anghinolfi, M. Ripani, S. Simula and M. Taiuti, Phys. Rev. C **57**, 356 (1998).

[18] F.E. Close and N. Isgur, Phys. Lett. B **509**, 81 (2001).

[19] A. De Rujula, H. Georgi and H.D. Politzer, Ann. Phys. **103**, 315 (1977); H. Georgi and H.D. Politzer, Phys. Rev. D **14**, 1829 (1976).

[20] E.D. Bloom and F.J. Gilman, Phys. Rev. D **4**, 2901 (1970).

[21] R.P. Feynman, *Photon Hadron Interactions* (Benjamin, Reading, Massachusetts, 1972); F.E. Close, Phys. Lett. **B43**, 422 (1973); Nucl. Phys. **B80**, 269 (1973); R.D. Carlitz, Phys. Lett. **B58**, 345 (1975); N. Isgur, Phys. Rev. D **59**, 034013 (1999).

[22] A.D. Martin, R.G. Roberts, W.J. Stirling and R.S. Thorne, Eur. Phys. J. C **14**, 133 (2000); H.L. Lai *et al.*, Eur. Phys. J. C **12**, 375 (2000); M. Glück, E. Reya and A. Vogt, Eur. Phys. J. C **5**, 461 (1998).

[23] G.R. Farrar and D.R. Jackson, Phys. Rev. Lett. **35**, 1416 (1975).

[24] S. Kuhlmann *et al.*, Phys. Lett. B **476**, 291 (2000).

[25] L.W. Whitlow *et al.*, Phys. Lett. B **282**, 475 (1992); A. Bodek, S. Dasu and S.E. Rock, in Tucson Part. Nucl. Phys., 768 (1991), SLAC-PUB-5598.

[26] W. Melnitchouk and A.W. Thomas, Phys. Lett. **B377**, 11 (1996).

[27] W. Melnitchouk and J.C. Peng, Phys. Lett. **B400**, 220 (1997).

[28] L.L. Frankfurt and M.I. Strikman, Nucl. Phys. **B250**, 1585 (1985); Phys. Rep. **160**, 235 (1988).

[29] W. Brooks, JLab E-94-017, www.jlab.org/exp_prog/proposals/94/PR94-017.pdf

[30] O. Gayou *et al.*, Phys. Rev. Lett. **88**, 092301 (2002); M.K. Jones *et al.*, Phys. Rev. Lett. **84**, 1398 (2000).

[31] S. Platchkov *et al.*, Nucl. Phys. A **510**, 740 (1990).

[32] L.L. Frankfurt and M.I. Strikman, Phys. Rep. **76**, 217 (1981).

[33] C. Ciofi degli Atti and S. Simula, Phys. Lett. **B319**, 23 (1993); Few-Body Systems **18**, 55 (1995); S. Simula, Phys. Lett. **B387**, 245 (1996); Few-Body Systems Suppl. **9**, 466 (1995).

[34] W. Melnitchouk, M. Sargsian and M.I. Strikman, Z. Phys. **A359**, 99 (1997).

[35] See e.g. R.P. Bickerstaff and A.W. Thomas, J. Phys. G **15**, 1523 (1989).

[36] W. Melnitchouk, A.W. Schreiber and A.W. Thomas, Phys. Lett. **B335**, 11 (1994); Phys. Rev. D **49**, 1183 (1994).

[37] G.D. Bosveld, A.E.L. Dieperink and A.G. Tenner, Phys. Rev. C **49**, 2379 (1994).

[38] F. Gross and S. Liuti, Phys. Rev. C **45**, 1374 (1992); S. Liuti and F. Gross, Phys. Lett. **B356**, 157 (1995).

[39] S.A. Kulagin, G. Piller and W. Weise, Phys. Rev. C **50**, 1154 (1994); S.A. Kulagin, W. Melnitchouk, G. Piller and W. Weise, Phys. Rev. C **52**, 932 (1995).

[40] S.I. Alekhin, S.A. Kulagin and S. Liuti, *in preparation*.

[41] L. Heller and A.W. Thomas, Phys. Rev. C **41**, 2756 (1990).

[42] S. Dieterich *et al.*, Phys. Lett. **B500**, 47 (2001); R. Ransome, Nucl. Phys. **A699**, 360 (2002).

[43] W. Melnitchouk, K. Tsushima, A.W. Thomas, Eur. Phys. J. A **14**, 105 (2002).

[44] L.L. Frankfurt *et al.*, Z. Phys. **A352**, 97 (1995); Phys. Lett. **B369**, 201 (1996).

[45] C. Ciofi degli Atti and B.Z. Kopeliovich, nucl-th/0207001.

[46] M.I. Strikman, M. Tverskoy and M. Zhalov, nucl-th/9609055, *Proceedings of Workshop "Future Physics at HERA"*, Hamburg, 1085 (1996).

[47] M.R. Adams *et al.*, Phys. Rev. Lett. **74**, 5198 (1995).

[48] C. Ciofi degli Atti, B.Z. Kopeliovich, Eur. J. Phys. *to appear*; nucl-th/0207001.

[49] A. Casher, H. Neuberger and S. Nussinov, Phys. Rev. D **20**, 179 (1979).

[50] B.Z. Kopeliovich, J. Nemchik and E. Predazzi, hep-ph/9511214, *Proceedings of the ELFE Summer School on Confinement Physics*, ed. S.D. Bass and P.A.M. Guichon, Editions Frontieres, Gif-sur-Yvette, 391 (1995).

[51] C. Ciofi degli Atti, L.P. Kaptari and D. Treleani, Phys. Rev. C **63**, 044601 (2001).

[52] C. Ciofi degli Atti, L.P. Kaptari and B.Z. Kopeliovich, *in preparation.*

[53] F.E. Close, R.G. Roberts and G.G. Ross Phys. Lett **B129**, 346 (1983).

[54] G.F. Chew and F.E. Low, Phys. Rev. **113**, 1640 (1959).

[55] L. Frankfurt, M. Sargsian and M. Strikman, *in preparation.*

[56] F. Sauli, *Development of High Gain GEM Detectors*, IEEE Nuclear Science Symposium 1998, Toronto, Canada; A. Sharma, *Gasseous Micropattern Detectors in Astrophyics, Radiology, and Plasma Physics*, IEEE Nuclear Science Symposium 2000, Lyon, France, and references therein; S. Bachman *et al.*, *High Rate X-ray Imaging using multi-GEM Detectors with a Novel Readout Design*, Vienna Conference on Instrumentation, (2001); S. Bachman *et al.*, Nucl. Instr. Meth. **A470**, 548 (2001).

[57] C. Altunbas *et al.*, Nucl. Instr. Meth. **A490**, 177 (2002); B. Ketzer *et al.*, *GEM Detectors for COMPASS*, IEEE Nuclear Science Symposium 2000, Lyon, France.

[58] F. Sauli, *private communication.*

[59] R.E. Bosch *et al.*, *The ALTRO Chip - Summary*, presented at the 2002 IEEE Nuclear Science Symposium in Norfok, VA.

[60] M.E. Christy *et al.*, (E94-110 Collaboration at JLab), publication in preparation.

[61] C. Keppel, *Proceedings of the Workshop on CEBAF at Higher Energies*, ed. N. Isgur and P. Stoler, 237, (1994).